Hydrological and climatological controls on radiocarbon concentrations in a tropical stalagmite

Franziska A. Lechleitner[1,2*], James U.L. Baldini[2], Sebastian F.M. Breitenbach[3], Jens Fohlmeister[4,5], Cameron McIntyre[1,6,7], Bedartha Goswami[8,9], Robert A. Jamieson[2], Tessa S. van der Voort[1], Keith Prufer[10], Norbert Marwan[8], Brendan J. Culleton[11], Douglas J. Kennett[11], Yemane Asmerom[12], Victor Polyak[12], Timothy I. Eglinton[1]

(1) Department of Earth Sciences, ETH Zurich, Sonneggstrasse 5, 8092 Zurich, Switzerland
(2) Department of Earth Sciences, Durham University, Durham, DH1 3LE, UK
(3) Department of Earth Sciences, Cambridge University, Downing Street, Cambridge, CB2 3EQ, UK
(4) Institute of Environmental Physics, University of Heidelberg, Im Neuenheimer Feld 229, 69129 Heidelberg, Germany
(5) Institute of Earth and Environmental Science, University of Potsdam, Karl-Liebknecht-Str. 24-25, 14476 Potsdam, Germany
(6) Department of Physics, Laboratory of Ion Beam Physics, ETH Zurich, 8093 Zurich, Switzerland
(7) Scottish Universities Environmental Research Centre (SUERC), East Kilbride, UK
(8) Potsdam-Institute for Climate Impact Research, Transdisciplinary Concepts & Methods, Telegraphenberg A 31, 14473 Potsdam
(9) Department of Physics, Universität Potsdam, Karl-Liebknecht-Str. 24-25, 14476 Potsdam, Germany
(10) Dept. of Anthropology, University of New Mexico, Albuquerque, NM 87106, USA
(11) Dept. of Anthropology, Institute for Energy and the Environment, The Pennsylvania State University, PA 16802, USA
(12) Dept. of Earth and Planetary Sciences, University of New Mexico, Albuquerque, NM 87131, USA

*Corresponding author: franziska.lechleitner@erdw.ethz.ch

Abstract

Precisely-dated stalagmites are increasingly important archives for the reconstruction of terrestrial paleoclimate at very high temporal resolution. In-depth understanding of local conditions at the cave site and of the processes driving stalagmite deposition is of paramount importance for interpreting proxy signals incorporated in stalagmite carbonate. Here we present a sub-decadally resolved dead carbon fraction (DCF) record for a stalagmite from Yok Balum Cave (southern Belize). The record is coupled to parallel stable carbon isotope

($\delta^{13}C$) and U/Ca measurements, as well as radiocarbon (^{14}C) measurements from soils overlying the cave system. Using a karst carbon cycle model we disentangle the importance of soil and karst processes on stalagmite DCF incorporation, revealing a dominant host rock dissolution control on total DCF. Covariation between DCF, $\delta^{13}C$, and U/Ca indicates that karst processes are a common driver of all three parameters, suggesting possible use of $\delta^{13}C$ and trace element ratios to independently quantify DCF variability. A statistically significant multi-decadal lag of variable length exists between DCF and reconstructed solar activity, suggesting that solar activity influenced regional precipitation in Mesoamerica over the past 1500 years, but that the relationship was non-static. Although the precise nature of the observed lag is unclear, solar-induced changes in North Atlantic oceanic and atmospheric dynamics may play a role.

1. Introduction

Stalagmites are critical archives for the reconstruction of terrestrial paleoclimate. They are dateable with exceptional precision, and provide high-resolution time series data that reflect past climatic and environmental conditions (e.g., Ridley et al., 2015a; Vaks et al., 2013). However, because local conditions that influence proxy signals can vary between cave sites, careful interpretation of stalagmite paleoclimate records is necessary. A robust interpretation of stalagmite paleoclimate proxies therefore requires detailed knowledge of surface and cave conditions, including cave monitoring studies (Breitenbach et al., 2015), and assessments of hydrological and carbon cycle processes within the karst system (Frisia et al., 2011; Noronha et al., 2015; Rudzka-Phillips et al., 2013).

Combined analyses of stable carbon isotopes and ^{14}C in stalagmite carbonate can be particularly informative because the two proxies reflect carbon inputs from different surface environment sources (atmosphere, soil and vegetation), and from the host rock (Genty et al., 2001; Hendy, 1971; Oster et al., 2010). Meteoric water encounters high CO_2 levels in the soil, epikarst, and bedrock atmosphere (Baldini, 2010; Breecker et al., 2012; Noronha et al., 2015). Due to the biological nature of the processes involved in the production of soil CO_2 (microbial decomposition of soil organic matter (SOM) and root respiration), the $\delta^{13}C$ is strongly depleted (around -26‰ for areas dominated by C_3-type plants), whereas ^{14}C is often slightly to moderately depleted compared to the contemporaneous atmosphere through the decomposition of older residual SOM (Suppl. Fig. 1) (Genty and Massault, 1999). Dissolution of the ancient (i.e., ^{14}C-free) carbonate host rock by the acidic aqueous solution results in higher $\delta^{13}C$ values but a further reduction in ^{14}C contents in the water solution (Suppl. Fig. 1) (Genty et al., 2001). Carbonate speleothems form when dripwater saturated with respect to $CaCO_3$ enters a cave, where CO_2 levels are generally much lower than in the dripwater solution (McDermott, 2004). CO_2 degassing leads to supersaturation in the solution with respect to $CaCO_3$ and subsequent carbonate precipitation. Rapid degassing, for example in well-ventilated caves or under slow drip rates, promotes kinetic isotopic fractionation effects, leading to substantially higher $\delta^{13}C$ values (Breitenbach et al., 2015; Frisia et al., 2011).

Early studies attempting to date groundwater using ^{14}C concluded that the composite origin of groundwater carbon leads to large age offsets compared to the contemporaneous atmosphere (Fontes and Garnier, 1979; Wigley, 1975), which is then transferred to stalagmite carbonate. The difference between the

91 stalagmite and the contemporaneous atmosphere ^{14}C content at the time of
92 carbonate deposition is called the 'dead carbon fraction' (DCF), and can be highly
93 variable depending on karst and soil conditions, such as the thickness of bedrock
94 overlying the cave and SOM age spectrum (Genty et al., 2001; Griffiths et al.,
95 2012; Noronha et al., 2014; Rudzka et al., 2011). Detailed understanding of
96 carbon cycle controls is therefore paramount for understanding specific karst
97 systems and for the correct interpretation of stalagmite proxy records.
98 Well-dated stalagmite ^{14}C time series have extended the IntCal calibration curve,
99 taking into account DCF as a constant offset between stalagmite ^{14}C
100 measurements and IntCal (Hoffmann et al., 2010; Southon et al., 2012). These
101 studies led to significant improvements in our ability to date natural and
102 archaeological samples in the absence of direct atmospheric ^{14}C records such as
103 tree rings (i.e., beyond 13.9 kyr BP) (Reimer et al., 2013). However, DCF
104 variations beyond the tree-ring based interval of the calibration curve are
105 difficult to account for and to distinguish from variations in atmospheric ^{14}C
106 activity, requiring a method independent from the calibration curve for the
107 detection of DCF variations in stalagmites. Although DCF may be relatively
108 constant in a cave environment over long periods of time (e.g., in stalagmite H-82
109 from Hulu Cave; Southon et al., 2012), significant short-term variations can occur
110 (Griffiths et al., 2012; Noronha et al., 2014), especially during climatic extremes
111 (e.g., the last deglaciation; Oster et al., 2010; Rudzka et al., 2011). Understanding
112 the factors driving DCF variations would not only be important for calibration
113 purposes, but might also open the door to ^{14}C dating of stalagmites using
114 conventional calibration approaches.
115

Here we present a sub-decadally resolved stalagmite ^{14}C record from the tropical Yok Balum Cave, Belize. The exceptional resolution and chronological precision of our ^{14}C record allows direct comparison to atmospheric ^{14}C activity over the past 1500 years, and provides valuable insights into how hydrology and the karst pathways respond to climatic changes at the site. We use $\delta^{13}C$ and U/Ca to infer the importance of kinetic fractionation and prior calcite precipitation (PCP) and/or prior aragonite precipitation (PAP) occurring at the site. Carbon cycle modeling and the analysis of soil samples from above the cave help disentangle the main processes influencing ^{14}C and $\delta^{13}C$ at our site and strengthen the proxy interpretation. We compare our high-resolution ^{14}C record to atmospheric ^{14}C from IntCal13 (Reimer et al., 2013) and solar activity proxies to detect similarities and infer driving mechanisms.

2. Cave setting and climate

Yok Balum Cave is located in southern Belize in the district of Toledo (16°12'30.780 N, 89°4'24.420 W, 366 m above sea level) (Fig. 1). The cave developed in a steep and remote hill in a SW-NE trending karst ridge composed of limestone of Cretaceous age of the Campur Formation (Kennett et al., 2012; Miller, 1996). The vegetation above the cave consists of dense subtropical forest, composed primarily of C3 plants. Soil thickness above Yok Balum Cave varies considerably; it is generally very thin (< 30 cm) but occasionally forms deeper (up to 60 cm) pockets in the strongly karstified limestone. The soil is a leptosol (WRB, 2006) and has poorly developed horizons. Due to the generally inaccessible location of the hilltop above Yok Balum Cave, it is unlikely that the vegetation and cave hydrology was ever disturbed by farming activities in the

141 past, although the area has been populated for millennia (Kennett et al., 2012;
142 Walsh et al., 2014).
143 Yok Balum Cave consists of a single main trunk conduit overlain by ~ 14 m of
144 karstified bedrock with one entrance at each end at different elevations,
145 resulting in constant airflow and a dynamic diurnal and seasonal ventilation
146 regime (Ridley et al., 2015a, 2015b) (Fig. 1). Detailed cave microclimate
147 monitoring, including logging of temperature, cave air CO_2, radon, and drip rates,
148 has been carried out since 2011 (Kennett et al., 2012; Ridley et al., 2015b). The
149 cave has a nearly constant temperature of 22.9 ± 0.5°C (Ridley et al., 2015b) that
150 closely reflects the outside mean annual air temperature. Belize is located at the
151 northernmost extent of the present-day boreal summer Intertropical
152 Convergence Zone (ITCZ), whose annual migration dominates local climate
153 (Ridley et al., 2015a) (Fig. 1). Precipitation is heavily biased towards the boreal
154 summer months, when 400-700 mm of monthly rainfall can be registered,
155 whereas winters are generally very dry (< 70 mm/month; Poveda et al., 2006).
156

157 **3. Materials and methods**

158 **3.1. Stalagmite YOK-I**

159 Stalagmite YOK-I was collected in 2006 and is 606.9 mm long. The upper 415
160 mm are entirely composed of aragonite and were analyzed previously for high
161 resolution stable isotopes of oxygen ($\delta^{18}O$) and $\delta^{13}C$ (Kennett et al., 2012) (Fig.
162 2). YOK-I was actively growing at the time of collection, and detailed U-Th
163 measurements indicate that the aragonitic section spans the last 2000 years
164 (Kennett et al., 2012). In this study, the top 285.5 mm of YOK-I were resampled
165 for ^{14}C, $\delta^{13}C$, and U/Ca.

3.2. Stalagmite ^{14}C measurements

Samples for high-precision graphite ^{14}C analysis were milled continuously along the growth axis, following the previous stable isotope sampling transect, using a semi-automated high-precision drill (Sherline 5400 Deluxe) at ETH Zürich. The resultant transect produced 198 high-precision ^{14}C measurements, taken at a resolution between 0.5 – 3.3 mm. Contamination from sample and equipment handling was minimized by cleaning all surfaces with methanol and drying using compressed air between each sample. Additionally, the top 0.1 mm of stalagmite surface was discarded after milling. Graphitization and ^{14}C analysis were performed at the Laboratory for Ion Beam Physics (LIP) at ETH Zürich. 8-12 mg aliquots of carbonate powder were graphitized using an automatic graphitization system fitted with a carbonate handling system (CHS-AGE, Ionplus) and ^{14}C content was measured with an accelerator mass spectrometer (MICADAS, Ionplus). Oxalic acid II (NIST SRM 4990C) was used as the normalizing standard and was measured to a precision better that 2‰. IAEA-C1 was used as blank while IAEA-C2 and a modern coral standard where used as secondary standards. A ^{14}C-free stalagmite sample was used as a processing control.

3.3. Stable isotope and trace element analysis

YOK-I was previously sampled at 100 µm resolution for $\delta^{13}C$ and $\delta^{18}O$ analysis, published in Kennett et al (2012). To avoid any depth bias during the re-sampling for the current study, stable isotope measurements were performed on aliquots from some of the same powders. This was especially important because

191 the age model based on the stable isotopes was applied to this study. Samples
192 were analyzed for $\delta^{18}O$ and $\delta^{13}C$ on a Thermo Delta V Plus mass spectrometer
193 coupled with a ThermoFinnigan GasBench II carbonate preparation device at the
194 Geological Institute, ETH Zürich, following the procedure described in
195 Breitenbach and Bernasconi (2011).
196 U/Ca ratios were measured on aliquots of the same powders used for ^{14}C and
197 $\delta^{13}C$. The powders were dissolved in 1% Nitric Acid (PWR 67% Nitric Acid
198 Ultrapure Normatom for trace element analysis, diluted with ultrapure water)
199 and measured using a Thermo Scientific X-Series II inductively-coupled plasma
200 mass spectrometer (ICP-MS) at Durham University. Multi-elemental Romil
201 standards and blanks were run throughout the sequence to allow precise
202 quantification and correction for machine drift. Analytical precision for U was
203 <5% RSD for individual measurements, and detection limits were generally <1
204 ppt. Ca measurement precision was generally <2% RSD, with all analyses well
205 above detection limits of ~<0.1ppb.
206
207 **3.4. Soil samples**
208 A ca. 60 cm deep soil profile, extending to the top of the bedrock, was collected in
209 June 2013. Because of the extreme karstification of the bedrock, soil thickness is
210 very variable above the cave, and a deeper pocket was chosen to capture the
211 maximum extent of the soil. The profile was sampled at 4-5 cm per sampled
212 depth for a total of 13 samples. All samples were stored in dark and cool
213 conditions whenever possible, and freeze-dried upon arrival to the laboratory.
214 Smaller aliquots of the soil samples were homogenized and larger plant
215 fragments particles (> 5 mm) were removed manually.

The amount of organic carbon and ^{14}C content in the soil profile was determined at LIP, ETH Zürich. To remove carbonates prior to analysis, aliquots of homogenized soil samples were transferred to silver capsules and fumigated over three days at 60°C using 37% HCl (puriss. p.a. grade, Sigma Aldrich) (Komada et al., 2008) and neutralized for 24 hrs over solid NaOH. Samples were then wrapped in a second tin capsule and pressed. The % organic carbon was determined using an elemental analyzer (Vario MICRO cube, Elementar) calibrated using atropine as the standard (Säntis, product SA990746B). ^{14}C content was determined on a second aliquot of carbonate-free soil containing 1 mg carbon using an automated graphitization system and an accelerator mass spectrometer (AGE-MICADAS, Ionplus). Oxalic acid II (NIST SRM 4990C) was the normalizing standard measured to 4‰ precision. Ancient anthracite coal was used as the blank and processing control and IAEA-C7 and -C8 were used as secondary standards. Samples where corrected for constant contamination by extraneous carbon using the anthracite processing control and secondary standards.

Water extractable organic carbon (WEOC) of the soil samples was characterized to infer the nature of SOM transported through the karst. ^{14}C content of WEOC was determined by extracting 5 g of soil with 20 ml of 0.5 wt% NaCl (in ultrapure water) in pre-combusted glass centrifuge tubes (similar to Hagedorn et al., 2004). The tubes were centrifuged three times for 15 min, and the solution was re-homogenized using a vortex mixer in between. The supernatant was decanted using combusted glass pipettes, filtered through a column containing a small amount of pre-combusted glass fibre to remove solid particles, and freeze-dried using a Christ Alpha 1-2 LD plus freeze-dryer equipped with an oil-free pump to

prevent contamination. The extracts were then transferred to pre-combusted 12 ml borosilicate Exetainer vials (Labco) using 5 ml of ultrapure water at pH 2. The ^{14}C content was measured following the method described in Lang et al. (2016) using wet chemical oxidation and accelerator mass spectrometry using a Gas Ion Source (GIS) interface (Ionplus).

3.5. Carbon isotope models

DCF in stalagmite YOK-I (DCF_{YOK-I}) reflects various sources, mainly soil and vegetation, carbonate host rock, and fractionation effects (Griffiths et al., 2012). In order to separate and infer the relative importance of each contributing source to DCF_{YOK-I}, a modified version of a soil-karst carbon isotope model, described in Fohlmeister et al. (2011) and Griffiths et al. (2012), was applied to the dataset (Suppl. Fig. 2). Briefly, the model first calculates the SOM spectrum that best fits the measured stalagmite bomb spike. Three SOM pools with different mean ages and turnover times were calculated, and optimized to find the best fit with the measured stalagmite bomb spike via a Monte Carlo approach (30,000 runs). The SOM spectrum was applied to the entire dataset to reveal the ^{14}C content of the soil gas. This assumes that vegetation and soil composition have remained constant over the period of stalagmite growth. Fractionation effects between CO_2 and HCO_3^- when entering the groundwater DIC solution are taken into account using the fractionation factor for ^{14}C $^{14}\varepsilon = 2 \times {}^{13}\varepsilon/10$ (Southon, 2011), resulting in approximately +1.8 fraction modern ($F^{14}C$; Reimer et al., 2004) at 25°C. The remaining DCF signal is divided into host rock dissolution and in-cave kinetic fractionation effects. In-cave kinetic fractionation ($\Delta\delta^{13}C$), including the effects of PCP/PAP, is calculated as the difference between

stalagmite $\delta^{13}C$ and $\delta^{13}C$ estimated for the drip water solution after carbonate dissolution, when water is saturated with respect to Ca^{2+} (Griffiths et al., 2012). Dripwater $\delta^{13}C$ can be calculated iteratively, by considering the host rock $\delta^{13}C$ and the soil-water DIC $\delta^{13}C$ (in our case 0‰ and -17‰, respectively). Using the DCF value at that point in time permits calculation of the relative contribution of the host rock and DIC to the total dripwater $\delta^{13}C$ (as described in Griffiths et al, 2012). Kinetic fractionation effects on ^{14}C are readily quantifiable, because a 1‰ change in $\delta^{13}C$ equals a shift of ca. 0.2 $F^{14}C$ in ^{14}C (Southon, 2011). After removing the effects of vegetation/SOM and kinetic fractionation, the residual DCF is attributed to host rock dissolution processes.

4. Results

4.1. YOK-I ^{14}C record

The YOK-I ^{14}C record extends from ~ -54 back to 1400 years BP (i.e., 2004 to 555 C.E.), based on the U/Th age model constructed by Kennett et al. (2012) (Table 1, Fig. 2). A gap is present between 1341 and 1400 C.E., due to sampling difficulties at the transition between two slabs of stalagmite YOK-I. The mean temporal resolution is 5 years, and the maximum resolution is 0.7 years. A general decay trend is visible between 555 and 1950 C.E., with superimposed deviations in the range of ±0.2 $F^{14}C$. The modern part of the ^{14}C record (1950-present, top 9.3 mm) shows a clear imprint of bomb carbon, with maximum values of 1.14 $F^{14}C$ (at 1990 C.E.) (Fig. 2B).

Conversion of ^{14}C activity to DCF reveals significant variability over the entire interval studied (Table 1, Fig. 3A). Errors in $DCF_{YOK\text{-}I}$ are between 0.23 and 0.67%, and were calculated using error propagation following Noronha et al.

(2014). DCF_{YOK-I} values range between 9.04 and 16.7% (mean: 12.9%). The lowest DCF values occur during the period ca. 700-1100 C.E., concurrent with the most enriched $\delta^{13}C$ values (Fig. 3C).

4.2. Stable isotopes and U/Ca

The new $\delta^{13}C$ record measured on aliquots of the samples used for ^{14}C and U/Ca analyses, is of a lower resolution but shows excellent agreement with the previous high-resolution profile published in Kennett et al. (2012), confirming that no spatial error occurred during the resampling (Table 1, Fig. 3C). Several pronounced positive excursions in $\delta^{13}C$ are apparent throughout the record, e.g., at ca. 1780, 1500, 940, 620, and most notably, between 1040-1100 C.E.

184 aliquots of powders drilled for ^{14}C analysis were also used for U/Ca measurements. Values (expressed as U/Ca in ppm/ppm × 1000) vary from 0.00068 to 0.02952, with a pronounced minimum during the period 1040-1100 C.E. and highest values at the beginning of the record (550-700 C.E.) (Table 1, Fig. 3B). A large gap in U/Ca measurements exists between ~ 1250-1600 C.E., due to the transition between two stalagmite slabs (as in the ^{14}C record), as well as lack of availability of sufficient sample powder for analysis. The early part of the record (550-1180 C.E.) is generally characterized by pronounced variability in U/Ca with several rapid (sub-decadal) large excursions synchronous with shifts in $\delta^{13}C$, whereas the more recent part (1600-1950 C.E.) shows much more uniform values.

4.3. Soil samples

315 Soil organic carbon (SOC) content was measured twice with similar results
316 (Table 2, Fig. 4, series A and B). The highest values are found in the top sample
317 (~20% organic carbon), mainly composed of plant litter in the organic horizon,
318 followed by a steady decrease towards the bottom of the profile, with the lowest
319 sample (at ~60 cm depth) only containing ~2% organic carbon.
320 $F^{14}C$ values from the bulk SOC are generally quite high (0.85 to 1.1 $F^{14}C$), with
321 systematically decreasing values towards the bottom of the profile (Table 2, Fig.
322 4). The presence of bomb carbon is suggested at the top of the profile, where the
323 highest values are found between 5-15 cm below the surface, whereas in the
324 topmost sample, $F^{14}C$ is slightly lower. The WEOC $F^{14}C$ shows a similar pattern as
325 the bulk soil, with a steady decrease in $F^{14}C$ from the top to the bottom of the
326 profile (0.93 to 1.09 $F^{14}C$). There is a bifurcation in WEOC and bulk SOC $F^{14}C$
327 values with increasing depth, with the WEOC fraction decreasing less rapidly and
328 implying younger carbon than in the bulk SOC (Table 2, Fig. 4).
329
330 **4.4. Karst carbon isotope modeling**
331 The model with the best fit to the bomb spike data from YOK-I (Fig. 5A) produces
332 a SOM spectrum with the following parameters:
333 y_1 = 6 years; c_1 = 34%
334 y_2 = 37 years; c_2 = 62%
335 y_3 = 580 years; c_3 = 4%
336 where y_i denotes the mean age of the SOM pools and c_i the relative contribution
337 of the SOM pools to the respired soil gas CO_2. Applying this spectrum to the
338 entire record shows that most of the atmospheric variation is expressed in the
339 soil gas, due to the young SOM spectrum (Fig. 5B). Nevertheless, soil gas ^{14}C

activity is ~0.01 $F^{14}C$ lower than the contemporaneous atmospheric ^{14}C activity, and lagging the latter by ~15 years (Fig. 5B), due to the integrating nature of SOM. A slight enrichment occurs due to fractionation effects between CO_2 and DIC in the soil. The average contribution from vegetation and SOM to DCF_{YOK-I} is 0.015 $F^{14}C$, whereas the average enrichment from in-cave fractionation is -0.027 $F^{14}C$. The host rock contribution is therefore dominant, amounting to 0.139 $F^{14}C$ on average (Fig. 5C).

5. Discussion

5.1. Sources of carbon in stalagmite YOK-I

We disentangle the influence of soil and karst processes on stalagmite carbon isotopes by combining high-precision isotope measurements on stalagmites, bulk SOC and soil WEOC, and karst carbon isotope modeling.

The trend towards lower ^{14}C activities in the soil profile (Fig. 4) reflects general ageing of the SOM related to gradual soil buildup, and the slow downward cycling of dissolved organic matter (DOM), as described in a conceptual model by Kaiser and Kalbitz (2012). In this model, temporary storage of DOM through sorption mechanisms and microbial degradation result in an increasing trend in SOM ^{14}C ages with depth. The WEOC represents the most labile pool of SOM that is readily dissolved in water (Hagedorn et al., 2004) and reflects the same trend as the bulk soil samples, but with a less pronounced decrease in ^{14}C content. This is likely related to the preferential extraction of smaller, and thus more labile, compounds from the soil, including those from living microbial biomass (Hagedorn et al., 2004; Jones and Willett, 2006).

364 The analysis of bulk soil and WEOC samples shows that the SOM spectrum from
365 the soil above Yok Balum is quite young, and that the DOM leached from the soil
366 matrix (WEOC) echoes this trend. Backward modeling of SOM from the bomb
367 spike in YOK-I corroborates a very young SOM contribution to the karst system
368 (96% <50 years old) (Fig. 5). Although the model assumes constant vegetation
369 type and density above Yok Balum Cave over the past 1500 years, vegetation
370 shifts may have occurred because of severe droughts recorded between 700-
371 1100 C.E. (Kennett et al., 2012). Less dense vegetation and reduced soil microbial
372 activity during dry periods or under sustained deforestation would result in
373 older apparent ages of the SOM and lead to stronger smoothing of the
374 atmospheric ^{14}C signal delivered to the cave and increased stalagmite DCF
375 (Fohlmeister et al., 2011a). However, this signal would be opposite than that
376 observed in $DCF_{YOK\text{-}I}$ during the 700-1100 C.E. period, where DCF is at its
377 minimum. We attribute this to the minor influence of SOM to $DCF_{YOK\text{-}I}$ (Fig. 5C),
378 and therefore we conclude that large changes in DCF cannot originate from SOM
379 variability.
380 Young and fast cycling soils are often observed at tropical sites (Trumbore,
381 1993), where high temperature and humidity promote biological activity and
382 consequently result in high SOM turnover rates (Davidson and Janssens, 2006).
383 On the other hand, studies from (sub-)tropical karst settings have suggested that
384 a substantial contribution from pools of pre-aged SOM must influence the carbon
385 cycle at these locations: at Liang Luar Cave, on the Indonesian island of Flores,
386 the modeled SOM was dominated by a multi-centennial carbon pool (Griffiths et
387 al., 2012). A very old SOM spectrum was also observed in a recent study on soils
388 from above Heshang Cave, China (Noronha et al., 2015). It is likely that

differences in local conditions, soil depth, and microbial activity, and the magnitude of pre-aged organic carbon reservoirs in the deep vadose zone, are responsible for the contrasting characteristics of the Yok Balum Cave speleothem.

The overall modeled contribution of SOM to the DCF_{YOK-I} is found to be small (max. 2.5%), and the largest contributions to DCF_{YOK-I} appear to come from carbonate dissolution in the karst and from changes in karst hydrology (Fig. 6C). Measured DCF_{YOK-I} shows substantial and rapid transitions of up to 4%, with lower DCF values correlating with less negative $\delta^{13}C$ and $\delta^{18}O$ values and vice-versa (Fig. 3). This suggests lower/higher DCF_{YOK-I} occurred during drier/wetter conditions, corroborating studies where stalagmite DCF was observed to co-vary with other hydroclimate proxies (Griffiths et al., 2012; Noronha et al., 2014). The hydrological imprint on DCF appears to be related to shifts between the open and closed end-members of the karst system (Hendy, 1971). More open system conditions prevail during periods of lower recharge, i.e. drier periods. This promotes lower DCF values as the karst aqueous solution constantly re-equilibrates with the soil CO_2 reservoir through air-filled voids and pores, resulting in higher water (and stalagmite) ^{14}C activities. Conversely, during wetter periods, the karst system is more often waterlogged and the aqueous solution becomes isolated from the contemporaneous soil CO_2 reservoir (closed system), resulting in much higher amounts of dead carbon from carbonate dissolution being added to the solution (Fohlmeister et al., 2011b).

The importance of kinetic fractionation and PCP/PAP with respect to carbon isotopic signatures in YOK-I are investigated using both $\delta^{13}C$ and U/Ca, coupled to modeling. We consider both processes; although YOK-I is aragonitic, PCP

414 could occur in the karst overlying the cave, increasing the Mg/Ca ratio in the
415 aqueous solution, and consequently resulting in aragonite precipitation in the
416 cave (Wassenburg et al., 2012). U sourced from the overlying soil and the host
417 rock itself can be modulated by PCP/PAP (Johnson et al., 2006). Because U is
418 incorporated in the carbonate lattice, PAP should effectively scavenge U from the
419 drip water solution, resulting in lower stalagmite U contents during drier
420 periods (Jamieson et al., *in press*; Wassenburg et al., *in press*). $\delta^{13}C$ is strongly
421 altered by kinetic in-cave fractionation and PCP/PAP, as forced degassing by low
422 CO_2 partial pressure enriches the solution in ^{13}C (Frisia et al., 2011; Hendy,
423 1971). Modeling of kinetic fractionation effects between DIC and $CaCO_3$ (both in-
424 cave fractionation and PCP/PAP) in stalagmite YOK-I shows that most of the
425 variation in $\delta^{13}C$ is attributable to this process, whereas the soil and carbonate
426 host rock signatures are only responsible for the overall range in $\delta^{13}C$ (Fig. 6).
427 Despite the fact that mass-dependent fractionation with respect to ^{12}C is about
428 twice as strong for ^{14}C than ^{13}C, fractionation effects are generally not as strongly
429 expressed in ^{14}C as in $\delta^{13}C$, due to the difference in unit of the two parameters (%
430 in ^{14}C vs. ‰ in $\delta^{13}C$) (Fohlmeister et al., 2011b; Southon, 2011). Most of the
431 variability in $\delta^{13}C$ attributed to fractionation by the karst model is also present in
432 the U/Ca record (Fig. 6B). Several large and rapid positive excursions are found
433 both in $\delta^{13}C$ and U/Ca, most notably between 1040 and 1100 C.E., and all
434 coincide with periods of increased in-cave kinetic fractionation as calculated
435 with $\Delta\delta^{13}C$. U/Ca ratios in YOK-I therefore are interpreted to reflect local
436 hydrological conditions and the amount of PAP occurring at the site, providing
437 additional evidence for kinetic fractionation as the main driver of $\delta^{13}C$ in this
438 stalagmite.

Previous studies have highlighted the potential of hydrological proxies for detecting past stalagmite DCF shifts: Rudzka et al. (2011) showed that shifts in DCF during the last deglaciation were matched by synchronous shifts in $\delta^{13}C$, implying a common forcing mechanism on the two proxies (e.g., effective infiltration or changes in mean SOM age). Another study combined DCF and Mg/Ca data measured on a tropical stalagmite and highlighted the importance of host rock dissolution processes for stalagmite DCF (Griffiths et al., 2012).

In YOK-I, both $\delta^{13}C$ and U/Ca values show remarkable similarities ($r = -0.83$, $p < 0.001$), suggesting a strong imprint of PCP/PAP and in-cave kinetic fractionation on both proxies. Comparison with $DCF_{YOK\text{-}I}$ reveals a significant correlation with respect to U/Ca ($r = 0.49$, $p < 0.001$) and $\delta^{13}C$ ($r = -0.5$, $p < 0.001$), suggesting a common forcing on all three proxies (Fig. 7). Since kinetic fractionation is not a strong component of $DCF_{YOK\text{-}I}$ (Fig. 5), another mechanism driven by the same forcing that controls U/Ca and $\delta^{13}C$ must exist. The modeling results confirm that, similar to previous studies, the dominant control on $DCF_{YOK\text{-}I}$ is the dissolution of host rock carbonate, driven by open vs. closed system conditions. All three processes (host rock dissolution, kinetic fractionation and PCP/PAP) are sensitive to effective infiltration within the karst, and thus ultimately driven by climatic conditions. Increasing aridity leads to more open-system conditions and enhanced PAP and kinetic fractionation, resulting in strong covariance between DCF, U/Ca and $\delta^{13}C$ (Fig. 7). This relationship highlights the potential usefulness of combined $\delta^{13}C$, trace element and ^{14}C records to infer past DCF variability. It may also be possibile to detect changing infiltration even when DCF cannot be readily calculated, i.e., during time intervals beyond the tree-ring based interval of the ^{14}C calibration curve or for ^{14}C dating applications. U/Ca

464 ratios are increasingly recognized as sensitive tracers for PAP in aragonitic
465 stalagmites (Jamieson et al., *in press*), and other trace elements have successfully
466 been used in calcitic samples (e.g., Mg/Ca, Griffiths et al., 2012).
467 Detailed analysis of the sources of carbon in YOK-I reveals a strong dependency
468 on both hydroclimate and the amount of effective infiltration into the karst
469 system. DCF, $\delta^{13}C$ and U/Ca all show a trend towards drier conditions during the
470 period 700-1100 C.E., a time interval previously described in conjunction with
471 the disintegration of Classic Maya political systems (Douglas et al., 2015; Haug et
472 al., 2003; Hodell et al., 1995; Kennett et al., 2012). Whereas $\delta^{18}O$ reflects the
473 amount of precipitation, moisture source and storm path length, $\delta^{13}C$ is a useful
474 local indicator of effective infiltration into the karst (Ridley et al., 2015a). All
475 factors driving $\delta^{13}C$ result in its enrichment during dry periods: reduced
476 vegetation density and soil microbial activity result in higher $\delta^{13}C$ values of the
477 soil water; more open-system conditions in the karst promote PCP/PAP and
478 kinetic fractionation, progressively enriching $\delta^{13}C$ in the aqueous solution.
479 Therefore, although the kinetic nature of the processes acting on $\delta^{13}C$ prevent
480 quantification of the hydrological deficit, $\delta^{13}C$ in YOK-I is a sensitive recorder of
481 infiltration dynamics.
482
483 **5.2. 'Bomb' radiocarbon signals YOK-I**
484 The young SOM contribution to the drip water at Yok Balum Cave is reflected in
485 the pronounced bomb spike in stalagmite YOK-I, which reaches its peak at 1.14
486 $F^{14}C$, with an overall spike of 0.27 $F^{14}C$ (Fig. 2B). Comparing this value to the
487 maximum $F^{14}C$ in the atmospheric Northern Hemisphere zone 2 record (1.98
488 $F^{14}C$ in 1963; Hua et al., 2013) confirms that YOK-I is a highly responsive

489 stalagmite in terms of carbon transfer, with a damping ratio, D, of 66.1%. D is
490 calculated as the difference between the highest and lowest bomb-^{14}C value in
491 the stalagmite, compared to the atmospheric value. In comparison to an
492 extensive study of a number of stalagmites by Rudzka-Phillips et al. (2013), YOK-
493 I shows one of the least dampened bomb spikes. The rapid increase in $F^{14}C$,
494 synchronous with the beginning of the bomb spike rise, also highlights the rapid
495 fluid transfer in the karst at Yok Balum Cave. These features could be related to
496 the much higher sampling resolution in YOK-I compared to other studies;
497 however, the strong similarity between the bomb spike recorded in YOK-I and
498 YOK-G, another stalagmite from the same cave (Ridley et al., 2015a), suggests
499 that the amplitude of the perturbation is real. The YOK-I bomb spike does not
500 show a pronounced maximum, but rather a rapid increase in ^{14}C activity until ca.
501 1970 C.E., followed by a plateau, until decrease slowly starts after ca. 1990 C.E,
502 very similar to YOK-G (Fig. 2B). It is worth noting that the measured drip rate for
503 stalagmite YOK-G was 30 times higher than for YOK-I, likely attributable to
504 different hydrological pathways in the karst overlying the cave (Ridley et al.,
505 2015a). This corroborates the notion that processes related to the turnover of
506 soil organic matter are responsible for the modulation of the bomb spike in
507 stalagmites (Genty and Massault, 1999; Rudzka-Phillips et al., 2013), rather than
508 changes in karst hydrology. The two stalagmite bomb spikes from Yok Balum
509 Cave and the resultant modeled SOM spectra support the results from the
510 analysis of soil and WEOC samples, indicating only minor contributions of old
511 recalcitrant carbon from the soil to the karst system. Compared again with the
512 study by Rudzka-Phillips et al. (2013), the stalagmites from Yok Balum Cave
513 show similar behavior to the samples from arid and warm sites, with sparse

514 vegetation and thin soils. Although southern Belize is not characterized by year-
515 round aridity, the boreal winter months are very dry, and infiltration in the karst
516 is significantly reduced (Ridley et al., 2015b). Together with the low carbon
517 storage potential of the soils overlying Yok Balum Cave, this may explain the
518 apparent similarity to the arid sites described in Rudzka-Phillips et al. (2013).
519
520 **5.3. Lagged solar influence on DCF**
521 Similarities are apparent when comparing DCF_{YOK-I} to proxies for solar activity
522 (which modulates the production rate of atmospheric ^{14}C; Abreu et al., 2013),
523 such as the total solar irradiance (dTSI) record by Steinhilber et al. (2009) (Fig.
524 8). A lag-correlation analysis was performed between YOK-I and the Steinhilber
525 dTSI record. The YOK-I DCF and $\delta^{13}C$ records were first estimated on the same
526 (uniformly sampled) time scale as that of the Steinhilber dTSI using a Bayesian
527 proxy estimation approach presented in Goswami et al. (2014). All records were
528 normalized to mean zero and unit standard deviation, following which a
529 millennial trend was removed and the resulting residuals were smoothed with a
530 Gaussian kernel of 5 years width. Pearson's cross correlation was then estimated
531 between the resulting smoothed residuals at different lags by shifting the YOK-I
532 datasets ahead of the dTSI data appropriately. Using a window of 450 years over
533 the data, the evolution of lagged correlation was obtained which helped
534 demarcate distinct time periods based on the behavior of the lagged correlation
535 values over time (Fig. 8B).
536 The analysis reveals the presence of statistically significant correlations with a
537 persistent lag between 30 and 50 years of DCF_{YOK-I} with respect to dTSI during
538 the period 900-1250 C.E. However, for the period after ~1250 C.E., we fail to

539 detect similar statistically significant correlations. The same analysis was also
540 performed on $\delta^{13}C$, yielding very similar results as $DCF_{YOK\text{-}I}$ (although the lag
541 extends between 10-50 years in this case) (Fig. 8B). These observations strongly
542 suggest that hydrologic change at Yok Balum Cave occurred several decades
543 after shifts in atmospheric ^{14}C content, induced by solar irradiance, and were not
544 a direct reflection of contemporaneous atmospheric ^{14}C. Rainfall at Yok Balum
545 Cave is largely controlled by the seasonal migration of the ITCZ, and due to the
546 cave's location at the present-day northern boundary of the annual ITCZ range,
547 stalagmites from the site are very sensitive to subtle southward ITCZ migration
548 (Ridley et al., 2015a). Because the ITCZ tracks the Earth's thermal equator, it
549 migrates in response to hemispheric and global temperature shifts (Schneider et
550 al., 2014), controlled by the strength of the Sun, which also modulates
551 atmospheric ^{14}C content. Two possible processes could induce a lagged response
552 to the atmospheric records in $DCF_{YOK\text{-}I}$:
553 i) The stalagmite DCF is influenced by a large pool of 'old' organic carbon derived
554 from the soil or deep vadose zone, or
555 ii) The lag is an actual reflection of a delayed response of rainfall patterns at Yok
556 Balum Cave to solar forcing on climate.
557 The presence of large amounts of old carbon in the karst system is unlikely,
558 because the model results (based on the YOK-I bomb spike) suggest otherwise.
559 In addition, the fact that the lagged response to solar forcing is detectable in both
560 DCF and $\delta^{13}C$ (and U/Ca) suggests that there is another factor influencing both
561 proxies. Numerous studies have found decadal-scale lags (on the order of 10-40
562 years) in the response of rainfall patterns to solar forcing (Kobashi et al., 2015;
563 Moffa-Sanchez et al., 2014; Shindell et al., 2001; Swingedouw et al., 2011; Waple

et al., 2002). It is possible that a similar delayed response of Mesoamerican rainfall to solar forcing results in the lag observed in DCF_{YOK-I}, especially prior to 1250 C.E. Although the precise nature of the observed lag is unclear, solar-induced changes in the amount of freshwater and/or sea ice delivered to the North Atlantic basin and subsequent feedbacks in oceanic and atmospheric dynamics (e.g., in the state of the North Atlantic Oscillation) may play a role (Kobashi et al., 2015; Swingedouw et al., 2011; Waple et al., 2002). A possible solar influence on drought occurrence in the Yucatan has previously been suggested by Hodell et al. (2001). The apparent weakening of the solar influence on the YOK-I record after 1250 C.E. suggests a shift in the mechanism responsible for the observed lag between solar activity and rainfall at Yok Balum Cave. Although the causes for the lagged response between DCF_{YOK-I} and solar activity remain unclear, we note that the breaking down of the lagged proxy-Sun relationship (potentially a complete decoupling between rainfall and solar activity) is broadly synchronous with the beginning of the Little Ice Age (LIA), a period of extensive cooling in the Northern Hemisphere (Mann et al., 2009). This could therefore reflect a decreased influence of solar activity on hydroclimate (at least in Mesoamerica) during the LIA, and emergence of a different dominant forcing on ITCZ position (e.g., volcanism, Miller et al., 2012). However, other climate reconstructions and more extensive research are required to verify this interpretation.

6. Conclusions

We present a comprehensive study of carbon cycling and the controls on stalagmite DCF at the tropical Yok Balum Cave, southern Belize. Subdecadal-scale

589 DCF, $\delta^{13}C$, and U/Ca records from stalagmite YOK-I covering the last 1500 years,
590 combined with bulk SOC, WEOC, and modeling analysis of ^{14}C, reveal the sources
591 of carbon incorporated in stalagmite YOK-I, and on the factors and processes that
592 give rise to variations in DCF:

593 • Overall, the largest contribution to total DCF_{YOK-I} is carbonate bedrock
594 dissolution in the karst, significantly modulated by hydrological
595 conditions. Contributions of SOM to the total DCF_{YOK-I} are relatively small,
596 due to the fast SOM turnover and low carbon storage potential of the soil.
597 Dynamic ventilation of the cave system and seasonal aridity in the region
598 results in strong kinetic fractionation effects and PAP acting on $\delta^{13}C$ and
599 U/Ca. We acknowledge, however, that our approach of using constant
600 vegetation and SOM parameters in the model might bear some
601 weaknesses and should be refined by future studies.

602 • We find a strong relationship between DCF, $\delta^{13}C$, and U/Ca, suggesting a
603 common forcing factor on all three proxies (i.e., hydroclimate conditions
604 above the cave). These results highlight the potential usefulness of $\delta^{13}C$
605 and trace element ratios to track changes in stalagmite DCF, and could
606 help detecting past shifts in DCF when no independent age control is
607 available (e.g., for periods beyond the tree-ring based interval of the
608 atmospheric ^{14}C calibration curve) or for stalagmite ^{14}C dating purposes.

609 • Comparison of the high-resolution DCF_{YOK-I} and $\delta^{13}C$ records to IntCal13
610 and solar records shows compelling similarity with a variable lag (10-50
611 years) in the response of YOK-I to the solar forcing. We suggest that
612 rainfall above the site was driven by solar forcing but with a lagged
613 response, and raise the possibility that solar forcing of ITCZ position

varies temporally, and becomes much less prominent after the transition into the LIA.

Acknowledgements:

The authors gratefully acknowledge generous help from the LIP staff members, especially L. Wacker during sample preparation and measurement. N. Haghipour is thanked for help during sample preparation and accelerator mass spectrometry analysis. A.E. Thompson from the Uxbenká Archaeological Project is thanked for providing the map of the study site. C. Ottley is thanked for the ICP-MS aspects of the research. F. Hagedorn from the Swiss Federal Institute for Forest, Snow, and Landscape research (WSL) is thanked for advice regarding the WEOC methodology. This research was supported by the European Research Council grant 240167 to JULB.

References:

Abreu, J.A., Beer, J., Steinhilber, F., Christl, M., Kubik, P.W., 2013. 10Be in ice cores and 14C in tree rings: Separation of production and climate effects. Space Sci. Rev. 176, 343–349. doi:10.1007/s11214-011-9864-y

Baldini, J.U.L., 2010. Cave atmosphere controls on stalagmite growth rate and palaeoclimate records. Geol. Soc. London, Spec. Publ. 336, 283–294. doi:10.1144/sp336.15

Breecker, D.O., Payne, A.E., Quade, J., Banner, J.L., Ball, C.E., Meyer, K.W., Cowan, B.D., 2012. The sources and sinks of CO 2 in caves under mixed woodland and grassland vegetation. Geochim. Cosmochim. Acta. doi:10.1016/j.gca.2012.08.023

639 Breitenbach, S.F.M., Bernasconi, S.M., 2011. Carbon and oxygen isotope analysis
640 of small carbonate samples (20 to 100 ug) with a GasBench II preparation
641 device. Rapid Commun. Mass Spectrom. 25, 1910–1914.
642 doi:10.1002/rcm.5052
643 Breitenbach, S.F.M., Lechleitner, F.A., Meyer, H., Diengdoh, G., Mattey, D., Marwan,
644 N., 2015. Cave ventilation and rainfall signals in dripwater in a monsoonal
645 setting – a monitoring study from NE India. Chem. Geol. 402, 111–124.
646 doi:10.1016/j.chemgeo.2015.03.011
647 Davidson, E.A., Janssens, I.A., 2006. Temperature sensitivity of soil carbon
648 decomposition and feedbacks to climate change. Nature 440, 165–173.
649 doi:10.1038/nature04514
650 Douglas, P.M.J., Pagani, M., Canuto, M. a., Brenner, M., Hodell, D. a., Eglinton, T.I.,
651 Curtis, J.H., 2015. Drought, agricultural adaptation, and sociopolitical
652 collapse in the Maya Lowlands. Proc. Natl. Acad. Sci. 201419133.
653 doi:10.1073/pnas.1419133112
654 Fohlmeister, J., Kromer, B., Mangini, A., 2011a. The influence of soil organic
655 matter age spectrum on the reconstruction of atmospheric 14C levels via
656 stalagmites. Radiocarbon 53, 99–115.
657 Fohlmeister, J., Scholz, D., Kromer, B., Mangini, A., 2011b. Modelling carbon
658 isotopes of carbonates in cave drip water. Geochim. Cosmochim. Acta 75,
659 5219–5228. doi:10.1016/j.gca.2011.06.023
660 Fontes, J., Garnier, J.-M., 1979. Determination of the initial 14C activity of the total
661 dissolved carbon: a review of the existing models and a new approach.
662 Water Resour. Res. 15, 399–413.
663 Frisia, S., Fairchild, I.J., Fohlmeister, J., Miorandi, R., Spötl, C., Borsato, A., 2011.

664 Carbon mass-balance modelling and carbon isotope exchange processes in
665 dynamic caves. Geochim. Cosmochim. Acta 75, 380–400.
666 doi:10.1016/j.gca.2010.10.021
667 Genty, D., Baker, A., Massault, M., Proctor, C., Gilmour, M., Pons-Branchu, E.,
668 Hamelin, B., 2001. Dead carbon in stalagmites: Carbonate bedrock
669 paleodissolution vs. ageing of soil organic matter. Implications for 13C
670 variations in speleotherms. Geochim. Cosmochim. Acta 65, 3443–3457.
671 doi:10.1016/S0016-7037(01)00697-4
672 Genty, D., Massault, M., 1999. Carbon transfer dynamics from bomb-14C and
673 d13C time series of a laminated stalagmite from SW France - Modelling and
674 comparison with other stalagmite records. Geochim. Cosmochim. Acta 63,
675 1537–1548. doi:10.1016/S0016-7037(99)00122-2
676 Goswami, B., Heitzig, J., Rehfeld, K., Marwan, N., Anoop, A., Prasad, S., Kurths, J.,
677 2014. Estimation of sedimentary proxy records together. Nonlinear Process.
678 Geophys. 21, 1093–1111. doi:10.5194/npg-21-1093-2014
679 Griffiths, M.L., Fohlmeister, J., Drysdale, R.N., Hua, Q., Johnson, K.R., Hellstrom,
680 J.C., Gagan, M.K., Zhao, J.X., 2012. Hydrological control of the dead carbon
681 fraction in a Holocene tropical speleothem. Quat. Geochronol. 14, 81–93.
682 doi:10.1016/j.quageo.2012.04.001
683 Hagedorn, F., Saurer, M., Blaser, P., 2004. A 13C tracer study to identify the origin
684 of dissolved organic carbon in forested mineral soils. Eur. J. Soil Sci. 55, 91–
685 100. doi:10.1046/j.1365-2389.2003.00578.x
686 Haug, G.H., Günther, D., Peterson, L.C., Sigman, D.M., Hughen, K.A., Aeschlimann,
687 B., 2003. Climate and the Collapse of the Maya civilization. Science (80-.).
688 299, 1731–1735. doi:10.2307/482941

689 Hendy, C.., 1971. The isotopic geochemistry of speleothems—I. The calculation of
690 the effects of different modes of formation on the isotopic composition of
691 speleothems and their applicability as palaeoclimatic indicators. Geochim.
692 Cosmochim. Acta 35, 801–824. doi:10.1016/0016-7037(71)90127-X
693 Hodell, D.A., Brenner, M., Curtis, J.H., Guilderson, T., 2001. Solar Forcing of
694 Drought Frequency in the Maya Lowlands. Science (80-.). 292, 1367–1370.
695 Hodell, D.A., Curtis, J.H., Brenner, M., 1995. Possible role of climate in the collapse
696 of Classic Maya civilization. Nature 375, 391–394.
697 Hoffmann, D.L., Beck, J.W., Richards, D. a., Smart, P.L., Singarayer, J.S., Ketchmark,
698 T., Hawkesworth, C.J., 2010. Towards radiocarbon calibration beyond 28 ka
699 using speleothems from the Bahamas. Earth Planet. Sci. Lett. 289, 1–10.
700 doi:10.1016/j.epsl.2009.10.004
701 Hua, Q., Barbetti, M., Rakowski, a Z., 2013. Atmospheric radiocarbon for the
702 period 1950-2010. Radiocarbon 55, 2059–2072.
703 doi:10.2458/azu_js_rc.v55i2.16177
704 Jamieson, R. a., Baldini, J.U.L., Brett, M.J., Taylor, J., Ridley, H.E., Ottley, C.J., Prufer,
705 K.M., Wassenburg, J.A., Scholz, D., Breitenbach, S.F.M., n.d. Intra- and inter-
706 annual uranium concentration variability in a Belizean stalagmite controlled
707 by prior aragonite precipitation: a new tool for reconstructing hydro-
708 climate using aragonitic speleothems. Rev. - Geochim. Cosmochim. Acta.
709 Johnson, K.R., Hu, C., Belshaw, N.S., Henderson, G.M., 2006. Seasonal trace-
710 element and stable-isotope variations in a Chinese speleothem: The
711 potential for high-resolution paleomonsoon reconstruction. Earth Planet.
712 Sci. Lett. 244, 394–407. doi:10.1016/j.epsl.2006.01.064
713 Jones, D.L., Willett, V.B., 2006. Experimental evaluation of methods to quantify

714 dissolved organic nitrogen (DON) and dissolved organic carbon (DOC) in
715 soil. Soil Biol. Biochem. 38, 991–999. doi:10.1016/j.soilbio.2005.08.012
716 Kaiser, K., Kalbitz, K., 2012. Cycling downwards - dissolved organic matter in
717 soils. Soil Biol. Biochem. 52, 29–32. doi:10.1016/j.soilbio.2012.04.002
718 Kennett, D.J., Breitenbach, S.F.M., Aquino, V.V., Asmerom, Y., Awe, J., Baldini, J.U.L.,
719 Bartlein, P., Culleton, B.J., Ebert, C., Jazwa, C., Macri, M.J., Marwan, N., Polyak,
720 V., Prufer, K.M., Ridley, H.E., Sodemann, H., Winterhalder, B., Haug, G.H.,
721 2012. Development and disintegration of Maya political systems in response
722 to climate change. 788, 788–791. doi:10.1126/science.1226299
723 Kobashi, T., Box, J.E., Vinther, B.M., Blunier, T., White, J.W.C., Nakaegawa, T.,
724 Andresen, C.S., 2015. Modern solar maximum forced late twentieth century
725 Greenland cooling. Geophys. Res. Lett. 42, 5992–5999.
726 doi:10.1002/2015GL064764
727 Komada, T., Anderson, M.R., Dorfmeier, C.L., 2008. Carbonate removal from
728 coastal sediments for the determination of organic carbon and its isotopic
729 signatures , δ 13 C and Δ 14 C : comparison of fumigation and direct
730 acidification by hydrochloric acid. Limnol. Oceanogr. Methods 6, 254–262.
731 Lang, S.Q., Mcintyre, C., Bernasconi, S.M., Früh-Green, G.L., Voss, B.M., Eglinton,
732 T.I., Wacker, L., 2016. Rapid 14C analysis of dissolved organic carbon in non-
733 saline waters. Radiocarbon.
734 Mann, M.E., Zhang, Z., Rutherford, S., Bradley, R.S., Hughes, M.K., Shindell, D.,
735 Ammann, C., Faluvegi, G., Ni, F., 2009. Global signatures and dynamical
736 origins of the Little Ice Age and Medieval Climate Anomaly. Science 326,
737 1256–1260. doi:10.1126/science.1177303
738 McDermott, F., 2004. Palaeo-climate reconstruction from stable isotope

739 variations in speleothems: A review. Quat. Sci. Rev. 23, 901–918.
740 doi:10.1016/j.quascirev.2003.06.021
741 Miller, G.H., Geirsdóttir, Á., Zhong, Y., Larsen, D.J., Otto-Bliesner, B.L., Holland,
742 M.M., Bailey, D.A., Refsnider, K.A., Lehman, S.J., Southon, J.R., Anderson, C.,
743 Björnsson, H., Thordarson, T., 2012. Abrupt onset of the Little Ice Age
744 triggered by volcanism and sustained by sea-ice/ocean feedbacks. Geophys.
745 Res. Lett. 39, n/a–n/a. doi:10.1029/2011GL050168
746 Miller, T.E., 1996. Geologic and hydrologic controls on karst and cave
747 development in Belize. J. Cave Karst Stud. 58, 100–120.
748 Moffa-Sanchez, P., Born, A., Hall, I.R., Thornalley, D.J.R., Barker, S., 2014. Solar
749 forcing of North Atlantic surface temperature and salinity over the past
750 millennium. Nat. Geosci. 7, 275–278. doi:10.1038/NGEO2094
751 Noronha, A.L., Johnson, K.R., Hu, C., Ruan, J., Southon, J.R., Ferguson, J.E., 2014.
752 Assessing influences on speleothem dead carbon variability over the
753 Holocene: Implications for speleothem-based radiocarbon calibration. Earth
754 Planet. Sci. Lett. 394, 20–29. doi:10.1016/j.epsl.2014.03.015
755 Noronha, A.L., Johnson, K.R., Southon, J.R., Hu, C., Ruan, J., McCabe-Glynn, S., 2015.
756 Radiocarbon evidence for decomposition of aged organic matter in the
757 vadose zone as the main source of speleothem carbon. Quat. Sci. Rev.
758 doi:10.1016/j.quascirev.2015.05.021
759 Oster, J.L., Montañez, I.P., Guilderson, T.P., Sharp, W.D., Banner, J.L., 2010.
760 Modeling speleothem δ13C variability in a central Sierra Nevada cave using
761 14C and 87Sr/86Sr. Geochim. Cosmochim. Acta 74, 5228–5242.
762 doi:10.1016/j.gca.2010.06.030
763 Poveda, G., Waylen, P.R., Pulwarty, R.S., 2006. Annual and inter-annual variability

764 of the present climate in northern South America and southern
765 Mesoamerica. Palaeogeogr. Palaeoclimatol. Palaeoecol. 234, 3–27.
766 doi:10.1016/j.palaeo.2005.10.031
767 Reimer, P., Bard, E., Bayliss, A., Beck, J.W., Blackwell, P.G., Bronk Ramsey, C., Buck,
768 C., Cheng, H., Edwards, R.L., Friedrich, M., Grootes, P.M., Guilderson, T.P.,
769 Haflidason, H., Hajdas, I., Hatté, C., Heaton, T.J., Hoffmann, D.L., Hogg, A.G.,
770 Hughen, K.A., Kaiser, K.F., Kromer, B., Manning, S.W., Niu, M., Reimer, R.W.,
771 Richards, D.A., Scott, E.M., Southon, J.R., Staff, R.A., Turney, C.S.M., van der
772 Plicht, J., 2013. IntCal13 and Marine13 Radiocarbon Age Calibration Curves
773 0–50,000 Years cal BP. Radiocarbon 55, 1869–1887.
774 doi:10.2458/azu_js_rc.55.16947
775 Reimer, P.J., Brown, T.A., Reimer, R.W., 2004. Discussion: reporting and
776 calibration of post-bomb 14C data. Radiocarbon 46, 1299–1304.
777 Ridley, H.E., Asmerom, Y., Baldini, J.U.L., Breitenbach, S.F.M., Aquino, V. V., Prufer,
778 K.M., Culleton, B.J., Polyak, V., Lechleitner, F. a., Kennett, D.J., Zhang, M.,
779 Marwan, N., Macpherson, C.G., Baldini, L.M., Xiao, T., Peterkin, J.L., Awe, J.,
780 Haug, G.H., 2015a. Aerosol forcing of the position of the intertropical
781 convergence zone since ad 1550. Nat. Geosci. 8, 195–200.
782 doi:10.1038/ngeo2353
783 Ridley, H.E., Baldini, J.U.L., Prufer, K.M., Walczak, I.W., Breitenbach, S.F.M., 2015b.
784 High-Resolution Monitoring of Yok Balum Cave , Belize : an Investigation of
785 Seasonal Ventilation Regimes and the Atmospheric and Drip-Flow Response
786 To a Local Earthquake. J. Cave Karst Stud. 77, 183–199.
787 doi:10.4311/2014ES0117
788 Rudzka-Phillips, D., McDermott, F., Jackson, a., Fleitmann, D., 2013. Inverse

789 modelling of the 14C bomb pulse in stalagmites to constrain the dynamics of
790 soil carbon cycling at selected European cave sites. Geochim. Cosmochim.
791 Acta 112, 32–51. doi:10.1016/j.gca.2013.02.032
792 Rudzka, D., McDermott, F., Baldini, L.M., Fleitmann, D., Moreno, A., Stoll, H., 2011.
793 The coupled d13C-radiocarbon systematics of three Late Glacial/early
794 Holocene speleothems; insights into soil and cave processes at climatic
795 transitions. Geochim. Cosmochim. Acta 75, 4321–4339.
796 doi:10.1016/j.gca.2011.05.022
797 Schneider, T., Bischoff, T., Haug, G.H., 2014. Migrations and dynamics of the
798 intertropical convergence zone. Nature 513, 45–53.
799 doi:10.1038/nature13636
800 Shindell, D.T., Schmidt, G.A., Mann, M.E., Rind, D., Waple, A., 2001. Solar forcing of
801 regional climate change during the Maunder Minimum. Science 294, 2149–
802 2152. doi:10.1126/science.1064363
803 Southon, J., 2011. ARE THE FRACTIONATION CORRECTIONS CORRECT : ARE
804 THE ISOTOPIC REACTIONS REALLY TWICE THOSE FOR 13 C / 12 C ? 53.
805 Southon, J., Noronha, A.L., Cheng, H., Edwards, R.L., Wang, Y., 2012. A high-
806 resolution record of atmospheric 14C based on Hulu Cave speleothem H82.
807 Quat. Sci. Rev. 33, 32–41. doi:10.1016/j.quascirev.2011.11.022
808 Steinhilber, F., Beer, J., Fröhlich, C., 2009. Total solar irradiance during the
809 Holocene. Geophys. Res. Lett. 36, 1–5. doi:10.1029/2009GL040142
810 Swingedouw, D., Terray, L., Cassou, C., Voldoire, a., Salas-Mélia, D., Servonnat, J.,
811 2011. Natural forcing of climate during the last millennium: Fingerprint of
812 solar variability. Clim. Dyn. 36, 1349–1364. doi:10.1007/s00382-010-0803-
813 5

814 Trumbore, S.E., 1993. Comparison of radiocarbon dynamics in tropical and
815 temperate soils using radiocarbon measurements. Global Biogeochem.
816 Cycles 7, 275–290.
817 Vaks, A., Gutareva, O.S., Breitenbach, S.F.M., Avirmed, E., Mason, A.J., Thomas, A.L.,
818 Osinzev, A. V, Kononov, A.M., Henderson, G.M., 2013. Speleothems Reveal
819 500,000-Year History of Siberian Permafrost. Science (80-.). 340, 183–186.
820 doi:10.1126/science.1228729
821 Walsh, M.K., Prufer, K.M., Culleton, B.J., Kennett, D.J., 2014. A late Holocene
822 paleoenvironmental reconstruction from Agua Caliente, southern Belize,
823 linked to regional climate variability and cultural change at the Maya polity
824 of Uxbenká. Quat. Res. (United States) 82, 38–50.
825 doi:10.1016/j.yqres.2014.01.013
826 Waple, A.M., Mann, M.E., Bradley, R.S., 2002. Long-term patterns of solar
827 irradiance forcing in model experiments and proxy based surface
828 temperature reconstructions. Clim. Dyn. 18, 563–578. doi:10.1007/s00382-
829 001-0199-3
830 Wassenburg, J.A., Immenhauser, A., Richter, D.K., Jochum, K.P., Fietzke, J.,
831 Deininger, M., Goos, M., Scholz, D., Sabaoui, A., 2012. Climate and cave
832 control on Pleistocene/Holocene calcite-to-aragonite transitions in
833 speleothems from Morocco: Elemental and isotopic evidence. Geochim.
834 Cosmochim. Acta 92, 23–47. doi:10.1016/j.gca.2012.06.002
835 Wassenburg, J.A., Scholz, D., Jochum, K.P., Cheng, H., Oster, J.L., Immenhauser, A.,
836 Richter, D.K., Häger, T., Jamieson, R. a., Baldini, J.U.L., Hoffmann, D.L.,
837 Breitenbach, S.F.M., n.d. Determination of aragonite trace element partition
838 coefficients from speleothem calcite-aragonite transitions. Rev. - Geochim.

839 Cosmochim. Acta.

840 Wigley, T.M.L., 1975. Carbon 14 dating of groundwater from closed and open

841 systems. Water Resour. Res. 11, 324. doi:10.1029/WR011i002p00324

842 WRB, 2006. World reference base for soil resources 2006. Rome.

843

844 **Tables:**

Sample ID	U/Th age (yr AD)	Age error (yr)	$F^{14}C$ meas.	$F^{14}C$ meas. error (abs.)	DCF (%)	DCF error (%)	U/Ca x1000	$\delta^{13}C$	$\delta^{18}O$
1.1	2004.6	19	1.0419	0.0045			0.015	-7.34	-3.44
1.2	2003.4	19	1.0708	0.0046			0.006		
1.3	2001.9	4	1.0833	0.0048			0.010		
1.4	2000.0	4	1.0973	0.0048			0.016	-8.77	-3.80
1.5	1997.8	4	1.1143	0.0048					
1.6	1995.4	4	1.1175	0.0048			0.015	-9.28	-3.67
1.7	1992.7	4	1.1268	0.0049					
1.8	1989.7	4	1.1390	0.0049					
1.9	1987.2	4	1.1311	0.0049					
1.10	1983.2	4	1.1323	0.0049					
1.11	1979.7	4	1.1259	0.0049			0.015		
1.12	1976.0	4	1.1085	0.0049					
1.13	1969.4	4	1.0890	0.0047			0.013		
1.14	1961.0	1	0.9836	0.0043			0.014		
1.15	1956.8	1	0.9205	0.0041			0.016	-8.31	-3.46
1.16	1955.7	1	0.8948	0.0032			0.015		
1.17	1954.7	1	0.8667	0.0031			0.013		
1.18	1952.5	1	0.8622	0.0031	11.65	0.33	0.017		
1.19	1948.8	1	0.8528	0.0025	12.57	0.27	0.017		
1.20	1944.1	1					0.015	-8.26	-3.70
1.21	1939.0	1					0.015		
1.22	1934.1	1					0.015		
1.23	1930.0	1	0.8568	0.0025	12.68	0.27	0.017		
1.24	1927.0	1	0.8635	0.0032	12.24	0.33	0.016		
1.25	1924.4	1					0.015	-7.92	-3.69
1.26	1921.4	1	0.8588	0.0025	12.74	0.27	0.016		
1.27	1916.7	1	0.8693	0.0031	11.95	0.32	0.019		
1.28	1908.0	1	0.8626	0.0025	12.64	0.27	0.015		
1.29	1904.6	1					0.014	-7.32	-3.23
1.30	1903.0	1	0.8662	0.0031	12.46	0.32	0.014		
1.31	1899.7	3	0.8590	0.0026	13.33	0.27	0.016		
1.32	1891.8	3					0.017		
1.33	1891.1	3	0.8627	0.0030	12.68	0.32	0.015		
1.34	1890.9	3					0.017	-7.97	-3.33
1.35	1890.7	3	0.8544	0.0025	13.52	0.27	0.016		
1.36	1890.6	3	0.8576	0.0030	13.19	0.32	0.016		
1.37	1890.5	3					0.016		

1.38	1890.4	3	0.8650	0.0026	12.44	0.28	0.015		
1.39	1890.3	3	0.8700	0.0031	11.94	0.32	0.015	-7.88	-3.38
1.40	1890.3	3	0.8700	0.0026	11.93	0.27	0.016		
1.41	1890.2	3					0.015		
1.42	1890.0	3	0.8757	0.0032	11.36	0.33	0.012		
1.43	1889.9	3	0.8759	0.0027	11.33	0.28	0.014		
1.44	1889.5	3					0.013		
1.45	1889.1	3	0.8772	0.0031	11.20	0.33	0.015	-7.59	-3.50
1.46	1888.4	3	0.8716	0.0025	11.75	0.27	0.013		
1.47	1885.6	3					0.012		
1.48	1881.0	3	0.8848	0.0034	10.38	0.36	0.013		
1.49	1876.6	3	0.8787	0.0026	10.84	0.28	0.016		
1.50	1873.3	3					0.016	-8.49	-3.56
1.51	1870.0	3	0.8740	0.0031	11.35	0.32	0.016		
1.52	1867.0	3					0.016		
1.53	1864.3	3	0.8789	0.0026	10.75	0.28	0.016		
1.54	1862.2	3	0.8824	0.0031	10.47	0.32	0.015		
1.55	1860.4	3					0.012	-6.90	-3.32
1.56	1858.8	3	0.8874	0.0027	9.92	0.28	0.012		
1.57	1857.3	3	0.8800	0.0030	10.68	0.32	0.012		
1.58	1856.0	3	0.8756	0.0026	11.11	0.28	0.014		
1.59	1854.7	3					0.014	-8.33	-3.88
1.60	1853.5	3	0.8791	0.0031	10.73	0.33	0.014		
1.61	1852.3	3					0.012		
1.62	1851.1	3	0.8796	0.0025	10.79	0.28	0.013		
1.63	1849.9	3	0.8796	0.0031	10.78	0.33	0.014		
1.65	1847.4	3					0.015		
1.66	1845.9	3	0.8813	0.0031	10.62	0.32		-8.15	-3.75
1.67	1844.3	3					0.015		
1.68	1842.4	3	0.8834	0.0026	10.33	0.28			
1.69	1840.4	3	0.8823	0.0031	10.42	0.33	0.014		
1.71	1837.3	3					0.015		
1.72	1836.2	3	0.8700	0.0030	11.78	0.32			
1.73	1835.3	4	0.8670	0.0025	12.07	0.27			
1.74	1834.5	4					0.016	-7.81	-3.65
1.78	1833.7	4	0.8680	0.0030	11.96	0.32	0.016		
1.80	1832.1	4						-7.75	-3.83
1.81	1830.8	4	0.8729	0.0030	11.68	0.32	0.013		
1.83	1827.5	4	0.8616	0.0025	12.75	0.27	0.016		
1.84	1825.3	4	0.8659	0.0030	12.29	0.32			
1.86	1821.0	4					0.012	-8.17	-3.45
1.87	1819.1	4	0.8636	0.0030	12.52	0.32			
1.88	1817.3	4	0.8617	0.0025	12.66	0.27			
1.89	1815.6	4					0.015		
1.90	1813.9	4	0.8619	0.0031	12.60	0.33			
1.92	1810.5	4						-7.25	-3.79
1.93	1808.8	4	0.8568	0.0030	12.89	0.32	0.014		
1.94	1807.2	4	0.8527	0.0025	13.10	0.27			
1.96	1803.8	4	0.8492	0.0029	13.43	0.32	0.015		
1.97	1802.1	4						-7.56	-3.44
1.98	1800.4	4	0.8568	0.0025	12.49	0.27			
1.101	1795.5	4	0.8616	0.0026	11.55	0.29			
1.102	1793.9	4	0.8742	0.0060	10.23	0.62	0.012	-6.57	-3.23

1.103	1791.8	4	0.8671	0.0040	10.91	0.42			
1.104	1789.0	4	0.8616	0.0040	11.45	0.42			
1.105	1784.0	4	0.8604	0.0026	11.62	0.28			
1.106	1778.7	4	0.8549	0.0040	12.50	0.42	0.014		
1.107	1772.9	4	0.8578	0.0042	12.39	0.43			
1.108	1766.7	4					0.014		
1.109	1760.3	4	0.8575	0.0039	12.58	0.41			
1.110	1753.9	4	0.8543	0.0023	12.84	0.25	0.013	-7.47	-3.48
1.112	1741.8	4	0.8585	0.0021	12.37	0.23	0.014		
1.113	1736.3	4	0.8610	0.0036	12.26	0.38			
1.114	1730.9	6					0.014		
1.115	1726.0	6	0.8580	0.0039	13.00	0.41		-7.95	-3.89
1.116	1721.4	6					0.013		
1.118	1714.0	6					0.015		
1.119	1704.7	6	0.8552	0.0039	13.36	0.41		-7.86	-3.77
1.120	1696.3	6					0.015		
1.121	1690.1	6	0.8559	0.0040	12.98	0.42			
1.122	1688.9	6	0.8572	0.0025	12.84	0.27	0.015		
1.124	1684.6	6	0.8520	0.0039	13.29	0.41	0.016		
1.125	1683.8	6	0.8516	0.0021	13.32	0.24		-7.45	-3.53
1.126	1683.1	6					0.014		
1.127	1682.4	6	0.8537	0.0039	12.85	0.41			
1.128	1681.7	6	0.8467	0.0048	13.57	0.50	0.015		
1.129	1681.1	6	0.8501	0.0039	13.21	0.41		-7.99	-4.30
1.130	1680.5	3	0.8389	0.0022	14.35	0.24			
1.131	1679.1	3	0.8496	0.0040	13.25	0.42			
1.132	1673.6	3	0.8468	0.0025	13.42	0.27			
1.133	1671.2	3	0.8509	0.0040	12.98	0.42			
1.134	1668.0	3	0.8405	0.0045	14.01	0.47			
1.135	1664.3	3	0.8491	0.0040	12.78	0.42		-8.19	-4.11
1.136	1661.1	3	0.8450	0.0026	13.03	0.28	0.017		
1.137	1656.3	3	0.8416	0.0036	13.32	0.38			
1.138	1652.4	3					0.013		
1.139	1648.7	3	0.8321	0.0033	14.12	0.35		-7.38	-3.46
1.140	1645.0	3	0.8349	0.0025	13.62	0.27	0.017		
1.141	1641.8	3	0.8264	0.0034	14.25	0.36			
1.142	1638.8	3					0.014		
1.143	1637.5	3	0.8375	0.0044	13.05	0.47			
1.144	1636.4	3	0.8313	0.0025	13.65	0.28	0.014		
1.145	1635.3	3	0.8363	0.0036	13.12	0.38			
1.146	1612.9	3					0.016	-7.76	-3.43
1.147	1611.4	3	0.8392	0.0036	12.25	0.39			
1.148	1610.2	3	0.8365	0.0026	12.51	0.28	0.017		
1.149	1608.6	3	0.8377	0.0036	12.37	0.39			
1.150	1606.6	3					0.020	-8.20	-3.98
1.151	1604.5	3	0.8312	0.0045	12.97	0.48			
1.152	1601.9	3	0.8362	0.0036	12.71	0.38	0.017		
1.153	1598.9	3	0.8278	0.0044	13.56	0.47			
1.154	1596.7	3	0.8387	0.0025	12.48	0.28	0.017		
1.155	1594.8	3	0.8353	0.0044	12.82	0.47		-8.06	-3.70
1.156	1593.4	3	0.8374	0.0036	12.58	0.39			
1.157	1591.4	3	0.8327	0.0047	13.23	0.50	0.015		
1.158	1589.9	3	0.8406	0.0026	12.39	0.28			

1.159	1588.4	3	0.8363	0.0045	12.83	0.48	0.015		
1.160	1587.0	3	0.8408	0.0036	12.39	0.39		-8.11	-3.63
1.161	1585.7	3	0.8351	0.0045	12.98	0.47			
1.162	1584.3	3	0.8424	0.0026	12.20	0.28			
1.163	1583.0	3	0.8348	0.0045	12.98	0.48			
1.164	1581.6	3	0.8395	0.0036	12.50	0.38			
1.165	1580.1	2	0.8619	0.0038	10.14	0.40		-8.15	-3.48
1.167	1577.0	2	0.8452	0.0045	11.94	0.48			
1.168	1575.3	2	0.8463	0.0036	11.80	0.39			
1.169	1573.4	2	0.8433	0.0045	12.09	0.47			
1.170	1571.2	2	0.8465	0.0025	11.86	0.28			
1.171	1568.4	2	0.8481	0.0036	11.66	0.39		-8.10	-3.75
1.172	1565.5	2	0.8478	0.0036	11.73	0.39			
1.173	1562.8	2	0.8458	0.0036	11.92	0.39			
1.175	1559.3	2	0.8374	0.0046	12.77	0.49		-8.23	-3.48
1.176	1558.2	2	0.8416	0.0036	12.32	0.39			
1.177	1557.3	2	0.8471	0.0036	11.92	0.38			
1.178	1556.5	2	0.8481	0.0027	11.81	0.29			
1.179	1550.1	2	0.8340	0.0034	13.32	0.37			
1.180	1548.6	2	0.8269	0.0035	14.04	0.38			
1.181	1545.3	2	0.8221	0.0037	14.55	0.40		-8.01	-4.55
1.182	1543.5	2	0.8074	0.0031	16.06	0.33			
1.183	1541.7	2	0.8098	0.0045	15.88	0.48			
1.185	1537.8	2	0.8097	0.0045	15.85	0.47		-8.25	-3.57
1.186	1535.7	2	0.8148	0.0025	15.38	0.27			
1.187	1533.5	2	0.8255	0.0035	14.25	0.37			
1.189	1529.1	2	0.8211	0.0034	14.70	0.37			
1.190	1526.7	2	0.8164	0.0025	15.06	0.27			
1.191	1524.4	2	0.8179	0.0034	14.88	0.37		-8.08	-3.51
1.193	1519.5	4	0.8159	0.0034	14.91	0.36			
1.194	1517.1	4	0.8191	0.0025	14.51	0.28			
1.195	1514.5	4	0.8080	0.0035	15.65	0.38		-7.90	-3.77
1.197	1509.5	4	0.8132	0.0034	15.02	0.37			
1.198	1506.9	4	0.8196	0.0025	14.41	0.29			
1.199	1504.3	4	0.8109	0.0036	15.29	0.39			
1.200	1501.7	4						-7.66	-3.84
1.201	1499.1	4	0.8061	0.0038	15.81	0.41			
1.202	1496.6	4	0.8125	0.0033	15.13	0.37		-7.10	-3.66
1.203	1494.0	4	0.8172	0.0024	14.61	0.28			
1.204	1481.2	4	0.8146	0.0035	14.69	0.39			
1.206	1472.4	4	0.8057	0.0033	15.54	0.37		-7.58	-4.02
1.207	1469.9	4	0.8043	0.0025	15.66	0.29			
1.208	1466.1	4	0.8038	0.0033	15.65	0.37			
1.209	1462.9	4						-7.77	-4.15
1.210	1459.6	4	0.8090	0.0036	15.04	0.40			
1.211	1456.3	4	0.8052	0.0025	15.39	0.29		-7.78	-4.06
1.212	1453.1	4	0.8097	0.0035	14.89	0.39			
1.213	1449.9	3						-7.89	-3.59
1.214	1446.7	3	0.8090	0.0034	14.58	0.38			
1.215	1443.7	3	0.8087	0.0024	14.58	0.29			
1.216	1429.4	3	0.7912	0.0021	15.90	0.26			
1.217	1427.3	3						-8.11	-3.72
1.218	1425.5	3	0.7981	0.0020	15.05	0.24			

1.219	1423.9	3	0.7994	0.0024	14.89	0.29			
1.220	1422.5	3	0.7980	0.0034	14.97	0.39		-8.45	-3.90
1.222	1419.9	3	0.7941	0.0033	15.36	0.37		-8.55	-3.83
1.223	1418.7	3	0.7926	0.0024	15.50	0.29			
1.224	1417.6	3	0.7932	0.0034	15.43	0.39			
1.225	1416.6	3						-8.94	-3.89
1.226	1415.5	4	0.7897	0.0033	15.69	0.38			
1.227	1413.4	4	0.7926	0.0025	15.36	0.29			
1.228	1404.0	4	0.7935	0.0033	14.91	0.38		-8.28	-3.62
hr-1	1341.4	4	0.7905	0.0039	14.88	0.44	0.009	-9.38	-4.22
hr-3	1326.8	4	0.7848	0.0029	15.57	0.34	0.006		
hr-5	1311.8	4	0.7731	0.0039	16.49	0.44	0.003	-10.12	-4.56
hr-7	1296.7	6	0.7816	0.0027	15.18	0.33	0.003		
hr-9	1280.0	6	0.7853	0.0040	14.18	0.46	0.001	-9.51	-4.32
hr-11	1260.8	6	0.7785	0.0026	14.21	0.33	0.001	-9.01	-4.21
hr-13	1240.4	6	0.7740	0.0039	14.41	0.45	0.001	-9.19	-4.32
hr-15	1220.2	6	0.7522	0.0026	16.68	0.32	0.001	-9.52	-4.31
hr-17	1201.5	6	0.7490	0.0038	16.67	0.44	0.004	-8.64	-3.93
hr-19	1185.5	6	0.7582	0.0038	15.58	0.44	0.005	-8.45	-4.10
hr-21	1172.8	7	0.7610	0.0038	15.21	0.45	0.015	-8.32	-3.83
hr-23	1161.6	7	0.7600	0.0038	15.10	0.45	0.018	-8.54	-3.88
hr-25	1151.6	7					0.015	-8.25	-3.70
hr-27	1142.5	7	0.7570	0.0038	14.96	0.46	0.019	-7.83	-3.71
hr-29	1133.8	7	0.7599	0.0039	14.74	0.46	0.018	-7.80	-3.70
hr-31	1125.4	7	0.7551	0.0038	15.26	0.46	0.018	-7.56	-3.61
hr-33	1119.3	7	0.7587	0.0041	14.73	0.49	0.018	-7.57	-3.63
hr-35	1113.1	7	0.7410	0.0120		1.36	0.019	-7.26	-3.54
hr-37	1106.5	7	0.7672	0.0058	13.72	0.67	0.018	-7.77	-3.68
hr-39	1099.5	7					0.008	-5.52	-3.13
hr-40	1095.8	7	0.7991	0.0024	10.19	0.31			
hr-41	1091.9	7	0.8057	0.0026	9.51	0.33	0.002		
hr-42	1087.8	7	0.8094	0.0024	9.04	0.32			
hr-43	1083.6	7	0.8075	0.0027	9.33	0.35	0.002	-4.72	-3.21
hr-44	1079.1	6	0.7993	0.0024	10.36	0.31			
hr-45	1074.2	6	0.7939	0.0025	11.05	0.32	0.008	-6.21	-3.07
hr-46	1068.7	6	0.7906	0.0024	11.43	0.31			
hr-47	1062.8	6	0.7883	0.0030	11.67	0.36			
hr-48	1056.5	6	0.7964	0.0024	10.78	0.30			
hr-49	1050.1	6	0.7921	0.0026	11.12	0.33	0.009	-6.20	-3.36
hr-50	1043.6	6	0.7853	0.0023	11.72	0.30			
hr-51	1037.1	6	0.7851	0.0026	11.57	0.33	0.012		
hr-53	1024.6	6	0.7769	0.0026	12.14	0.33	0.013		
hr-55	1013.7	6	0.7707	0.0026	12.29	0.33	0.014		
hr-59	996.4	5	0.7731	0.0027	11.96	0.34	0.014		
hr-61	988.3	5	0.7768	0.0029	11.37	0.37	0.015		
hr-63	980.7	5	0.7754	0.0029	11.27	0.37	0.015		
hr-65	973.5	5	0.7756	0.0026	11.16	0.33	0.015		
hr-67	965.3	5	0.7763	0.0028	10.86	0.35	0.014	-8.35	-3.41
hr-69	956.5	5					0.014	-8.23	-3.54
hr-71	948.7	5	0.7771	0.0025	10.69	0.33	0.016	-7.55	-3.53
hr-73	941.9	10	0.7752	0.0026	10.77	0.37	0.015	-7.87	-3.78
hr-75	935.4	10	0.7787	0.0025	10.26	0.36	0.014	-7.26	-3.43
hr-77	931.0	9	0.7730	0.0025	10.97	0.35	0.015	-7.75	-3.89

hr-79	928.1	9	0.7585	0.0025	12.61	0.35	0.015	-7.77	-3.84
hr-81	924.1	9	0.7546	0.0025	13.19	0.35	0.015	-8.03	-3.68
hr-83	893.0	9	0.7533	0.0025	13.25	0.34	0.014	-7.70	-3.28
hr-85	850.9	9	0.7554	0.0025	12.30	0.35	0.017	-7.06	-3.33
hr-86	841.8	15	0.7633	0.0033	11.46	0.47			
hr-87	837.6	15	0.7625	0.0025	11.51	0.40	0.015	-7.48	-3.74
hr-88	832.9	15	0.7559	0.0032	12.31	0.46			
hr-89	829.4	15	0.7549	0.0027	12.43	0.41	0.017	-8.66	-4.09
hr-90	826.5	15	0.7591	0.0033	11.93	0.46			
hr-91	824.0	15	0.7539	0.0024	12.51	0.39	0.018	-8.43	-3.79
hr-92	821.8	15	0.7584	0.0032	12.00	0.46			
hr-93	819.8	15	0.7670	0.0025	10.99	0.40	0.017	-8.33	-3.45
hr-94	817.0	7	0.7700	0.0034	10.67	0.43			
hr-95	814.3	7	0.7663	0.0025	11.07	0.35	0.020	-8.10	-3.99
hr-96	811.8	7	0.7689	0.0033	10.81	0.42			
hr-97	809.5	7	0.7721	0.0025	10.41	0.34	0.018	-8.34	-3.53
hr-98	807.3	7	0.7724	0.0033	10.39	0.42			
hr-99	805.4	10	0.7701	0.0025	10.64	0.35	0.015	-7.97	-3.69
hr-100	803.7	10	0.7662	0.0033	11.07	0.43			
hr-101	801.9	10	0.7650	0.0025	11.18	0.36	0.018	-7.94	-3.55
hr-102	800.1	10	0.7673	0.0033	10.89	0.43			
hr-103	798.1	10	0.7594	0.0025	11.79	0.35	0.015	-8.04	-3.53
hr-104	796.1	10	0.7594	0.0032	11.78	0.42			
hr-105	793.8	10	0.7571	0.0027	12.03	0.37	0.016		
hr-107	788.3	13					0.018	-8.28	-3.80
hr-108	784.1	13	0.7534	0.0051	12.75	0.64			
hr-109	779.0	13					0.019	-7.94	-4.16
hr-110	773.1	13	0.7565	0.0051	12.06	0.64			
hr-111	766.7	13	0.7627	0.0026	10.70	0.38	0.021	-8.30	-3.95
hr-112	760.0	13	0.7650	0.0052	10.23	0.66			
hr-113	753.0	13	0.7720	0.0026	9.37	0.39	0.022	-8.50	-4.08
hr-114	749.6	13	0.7682	0.0052	9.88	0.65			
hr-115	746.1	13	0.7644	0.0026	10.46	0.38	0.020	-8.28	-4.09
hr-116	742.8	13	0.7704	0.0053	9.72	0.66			
hr-117	739.4	13	0.7684	0.0027	10.14	0.40	0.017	-8.27	-3.67
hr-118	736.2	13	0.7695	0.0054	10.19	0.67			
hr-119	733.1	13	0.7619	0.0026	11.04	0.39	0.016	-8.07	-3.95
hr-120	730.2	13	0.7577	0.0051	11.55	0.64			
hr-121	727.4	13	0.7554	0.0026	11.74	0.39	0.019		
hr-122	724.9	13	0.7512	0.0051	12.21	0.64			
hr-123	722.5	13	0.7499	0.0026	12.34	0.39	0.020	-8.34	-4.16
hr-124	720.4	13	0.7469	0.0052	12.63	0.66			
hr-125	718.6	13	0.7439	0.0026	12.96	0.39	0.016	-8.00	-3.96
hr-126	716.9	7	0.7559	0.0051	11.51	0.63			
hr-127	715.5	7	0.7544	0.0027	11.68	0.35	0.013	-7.16	-3.77
hr-128	714.1	7	0.7486	0.0051	12.34	0.62			
hr-129	712.8	7					0.020		
hr-131	710.3	7					0.018		
hr-133	707.7	7					0.022		
hr-134	706.3	7	0.7408	0.0050	13.19	0.61			
hr-135	704.8	7					0.023		
hr-136	703.2	7	0.7345	0.0051	13.90	0.62			
hr-137	701.3	7					0.023		

hr-138	699.2	7	0.7311	0.0046	14.32	0.57			
hr-139	697.0	7	0.7303	0.0026	14.45	0.35	0.022	-8.85	-4.35
hr-140	694.6	7	0.7344	0.0048	13.95	0.59			
hr-141	692.1	7	0.7371	0.0026	13.56	0.35	0.022		
hr-142	687.0	7	0.7387	0.0046	13.24	0.57			
hr-143	682.0	7	0.7317	0.0026	13.96	0.36	0.023	-8.55	-3.73
hr-144	677.4	7	0.7351	0.0047	13.47	0.58			
hr-145	673.2	7					0.023		
hr-146	669.1	7	0.7377	0.0046	13.02	0.57			
hr-147	665.0	7	0.7272	0.0026	14.10	0.35	0.020	-9.21	-4.36
hr-148	661.0	7	0.7288	0.0046	13.73	0.57			
hr-149	657.0	7	0.7266	0.0026	13.79	0.35	0.019	-8.36	-4.16
hr-150	653.1	7	0.7285	0.0045	13.53	0.56			
hr-151	649.2	7	0.7233	0.0026	13.95	0.35	0.017	-8.42	-3.92
hr-152	645.4	7	0.7245	0.0046	13.63	0.57			
hr-153	641.6	7	0.7173	0.0026	14.35	0.35	0.019	-9.43	-4.17
hr-154	637.8	7	0.7181	0.0045	14.21	0.56			
hr-155	634.0	7	0.7145	0.0025	14.56	0.34	0.017	-9.54	-4.27
hr-156	631.3	7	0.7130	0.0044	14.74	0.55			
hr-157	628.7	7	0.7203	0.0025	13.83	0.35	0.019	-9.11	-4.20
hr-158	626.0	7	0.7186	0.0045	14.06	0.56			
hr-160	620.8	7	0.7160	0.0045	14.35	0.56			
hr-161	618.1	7	0.7133	0.0024	14.64	0.34	0.014	-8.23	-3.56
hr-163	612.8	7	0.7196	0.0025	13.83	0.35	0.012	-7.38	-3.51
hr-165	607.5	7	0.7118	0.0024	14.70	0.34	0.018	-8.58	-3.58
hr-166	604.8	7	0.7098	0.0044	14.89	0.56			
hr-167	602.1	7					0.022	-9.26	-4.09
hr-169	596.6	7	0.7128	0.0025	14.32	0.34	0.021	-8.62	-3.93
hr-171	591.1	7	0.7161	0.0024	13.88	0.34	0.018	-8.53	-3.73
hr-173	585.6	9	0.7175	0.0025	13.70	0.35	0.022	-8.02	-3.58
hr-175	580.3	9	0.7036	0.0024	15.34	0.35	0.028	-10.11	-4.04
hr-177	575.2	9	0.7088	0.0024	14.67	0.35	0.023	-10.39	-3.97
hr-179	570.3	9	0.7103	0.0024	14.42	0.35	0.030	-9.94	-4.08
hr-181	565.5	9	0.7113	0.0024	14.23	0.34	0.023	-10.45	-4.16
hr-183	560.5	9	0.7113	0.0024	14.17	0.35	0.025	-9.74	-3.98
hr-185	555.5	9	0.7130	0.0024	13.90	0.35	0.024	-9.59	-3.78

Table 1: Results of the proxy study on stalagmite YOK-I. DCF was calculated using the formula: $\boldsymbol{DCF = 1 - \left(a^{14}C_{stal.init.} / a^{14}C_{atm.init.} \right)}$ where $a^{14}C_{stal.\ init.}$ and $a^{14}C_{atm.\ init.}$ represent stalagmite and atmosphere ^{14}C activity (respectively) at the time of carbonate deposition.

Sample name	Depth (cm)	Amount C (%) series A	Amount C (%) series B	$F^{14}C$ bulk soil	error (abs.)	WEOC DOC (mg/L)	$F^{14}C$ WEOC	error (abs.)
YB_S1	0	13.3	22.8	1.0749	0.0043	16.6	1.0640	0.0098
YB_S2	5	14.9	13.4	1.0996	0.0044	15.2	1.1117	0.0100
YB_S3	10	11.7	9.3	1.0986	0.0043	17.2	1.1179	0.0107
YB_S4	15	7.0	6.6	1.0820	0.0043	14.2	1.1165	0.0103
YB_S5	20	4.9	7.6	1.0507	0.0041	9.8	1.0926	0.0101
YB_S6	25	4.2	4.7	1.0063	0.0040	7.6	1.0876	0.0098
YB_S7	30	4.7	5.7	0.9818	0.0041	8.0	1.0619	0.0095
YB_S8	35	4.6	7.5	0.9726	0.0040	7.1	1.0610	0.0099
YB_S9	40	3.5	3.8	0.9552	0.0039	6.1	1.0414	0.0097
YB_S10	45	2.7	3.5	0.9216	0.0037	6.2	1.0041	0.0094
YB_S11	50	2.6	0.0	0.8851	0.0037	6.7	0.9853	0.0092
YB_S12	55	4.2	3.7			4.5	0.9805	0.0092
YB_S13	60	2.3	1.9	0.8572	0.0035	8.2	0.9456	0.0092

Table 2: Analysis of soil samples. A profile consisting of 13 samples was collected above Yok Balum Cave, and both bulk SOC and WEOC ^{14}C were measured.

Figures:

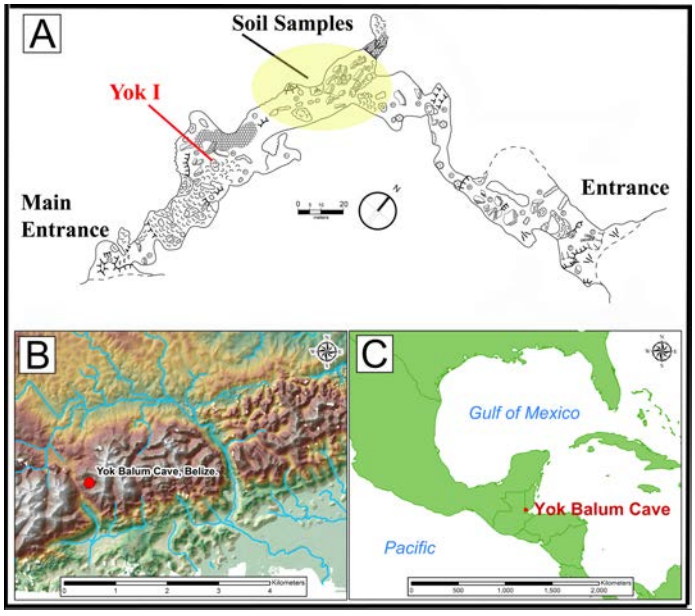

Fig. 1. Maps of Yok Balum cave, southern Belize: A - Cave map showing the location of stalagmite YOK-I (red dot), and the approximate position of the soil profile collected above the cave (yellow circle) (Map A is adapted from a map by

Tom Miller). B - Topographic map of the study site, with indication of the location of Yok Balum cave. C - Overview map of Central America and the general setting of the cave. (Maps in B and C are by A.E. Thompson, courtesy of the Uxbenká Archaeological Project).

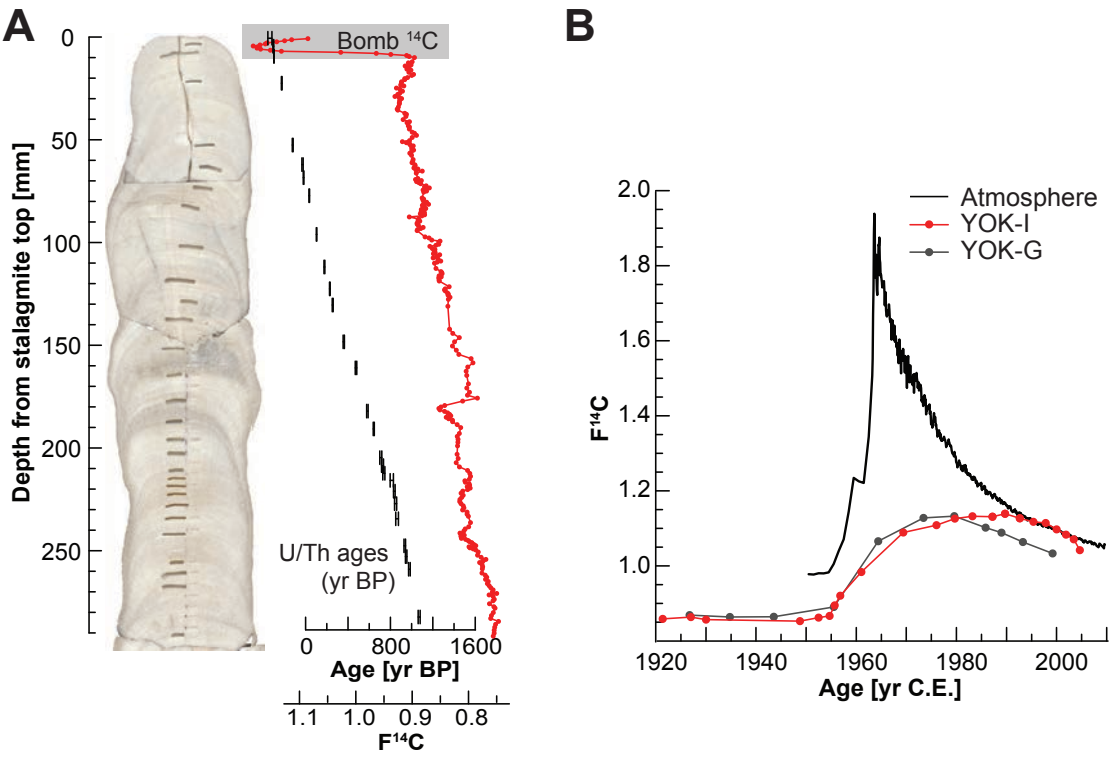

Fig. 2: A - Photoscan of the section of stalagmite YOK-I that was analysed for ^{14}C together with results from ^{14}C analysis (U/Th ages are shown for comparison). A pronounced bomb spike appears at the top of the stalagmite. B - Bomb spike recorded in stalagmite YOK-I (red dots), compared to the atmospheric record from the northern Hemisphere zone 2 (Hua et al. (2013), black line), and to the bomb spike recorded in stalagmite YOK-G from the same cave (grey dots, Ridley et al. (2015a)). Signal damping due to the age spectrum of SOM results in the lower amplitude and slightly delayed response of stalagmites YOK-I and YOK-G with respect to the atmosphere.

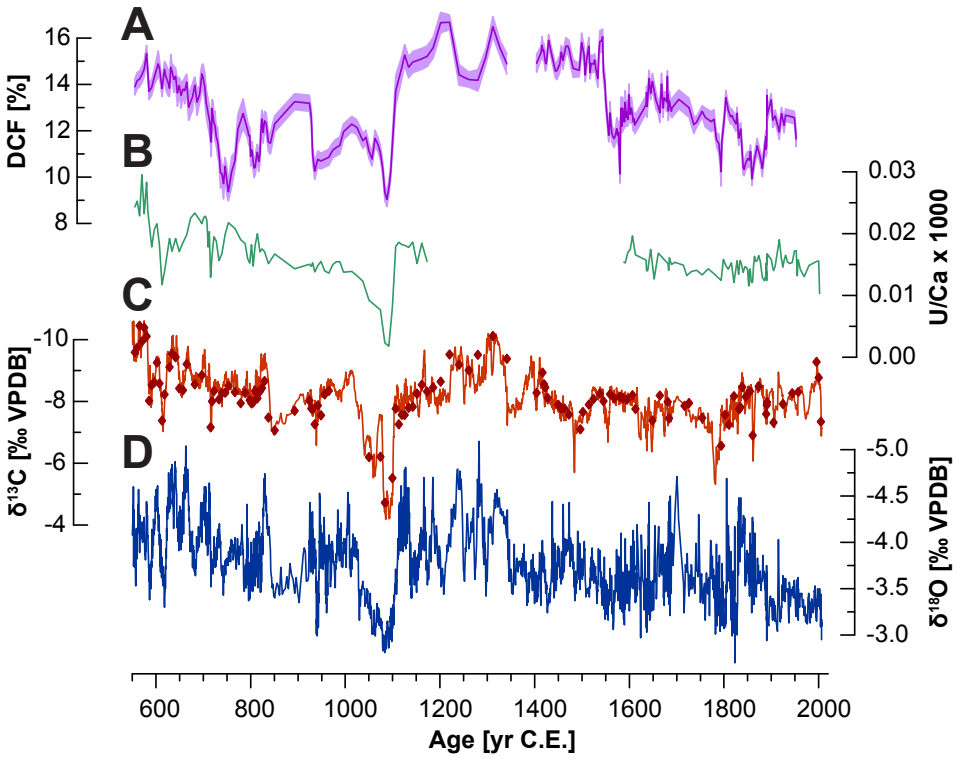

Fig. 3: Results of the analysis of geochemical proxies in stalagmite YOK-I: A - DCF calculated from ^{14}C measurements (purple line, including 1σ errors); B - U/Ca in ppm/ppm x 1000 (green line); C - $\delta^{13}C$ measured on the same aliquots as used for ^{14}C analysis (dark red diamonds) show that no sampling bias occurred with respect to the original high-resolution $\delta^{13}C$ time series (light red line); D - $\delta^{18}O$ from the original high-resolution time series (both high resolution stable isotope records were previously published in Kennett et al., 2012).

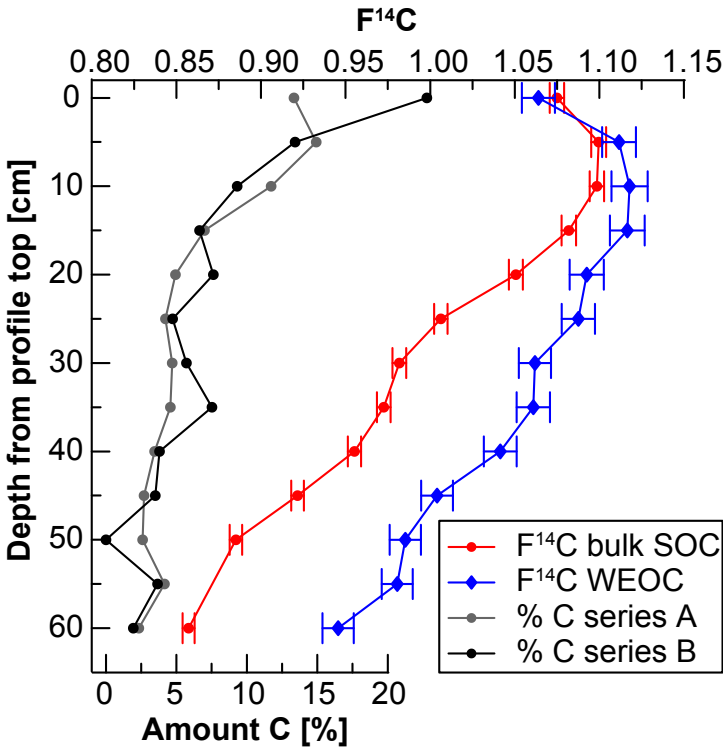

886

887 Fig. 4: Results from the analysis of the soil profile collected above Yok Balum
888 cave. Amount of carbon present in the samples was determined twice, showing
889 very reproducible results (grey and black dots). $F^{14}C$ shows regularly decreasing
890 values through the bulk SOC profile with bomb carbon imprint in the top 10 cm
891 (red dots), and a slower decrease in the WEOC (blue dots).

892

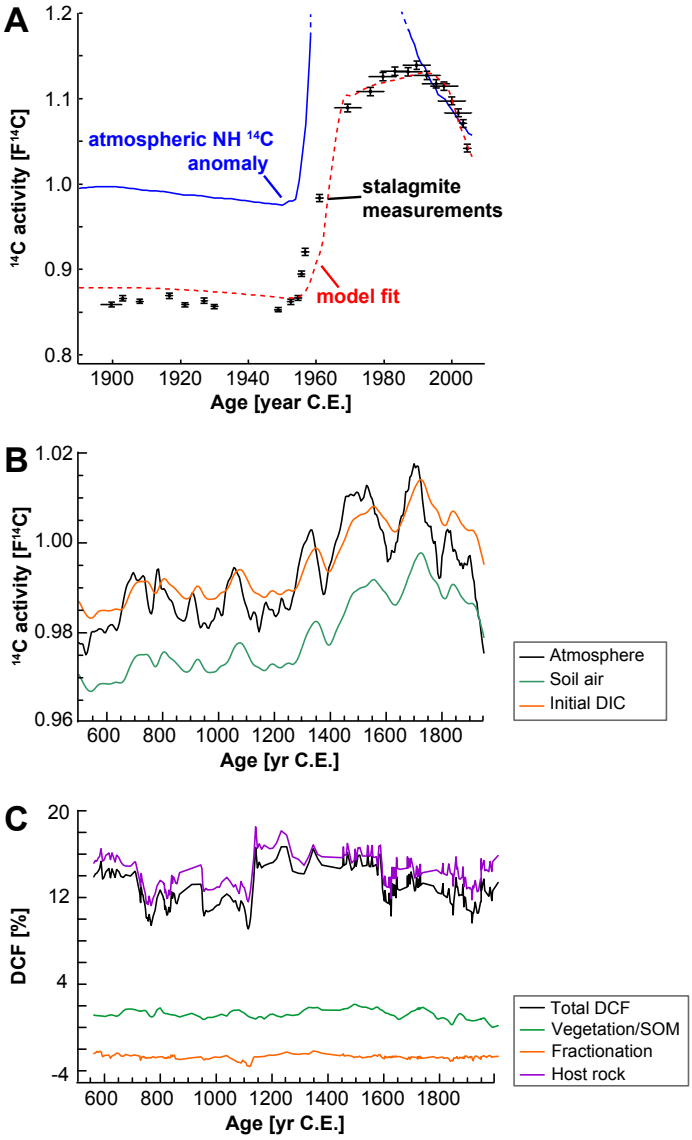

Fig. 5: Results of the modeling procedure on stalagmite YOK-I: A - The best fit of the model with the bomb spike data (black symbols) is shown by the red dashed line, the atmospheric bomb spike is shown for comparison in blue. B - The calculated soil air ^{14}C activity, after applying the SOM spectrum derived from the bomb spike on the entire time series, is shown in green. Fractionation between gaseous CO_2 and DIC results in slight enrichment (orange line). The atmospheric activity is shown in black for comparison. C - Results of the deconvolution of DCF: the black line shows the total DCF as measured on the stalagmite. The DCF contribution from vegetation/SOM is shown by the green line, and in-cave

fractionation effects result in the orange line. DCF derived from host rock dissolution is shown in purple.

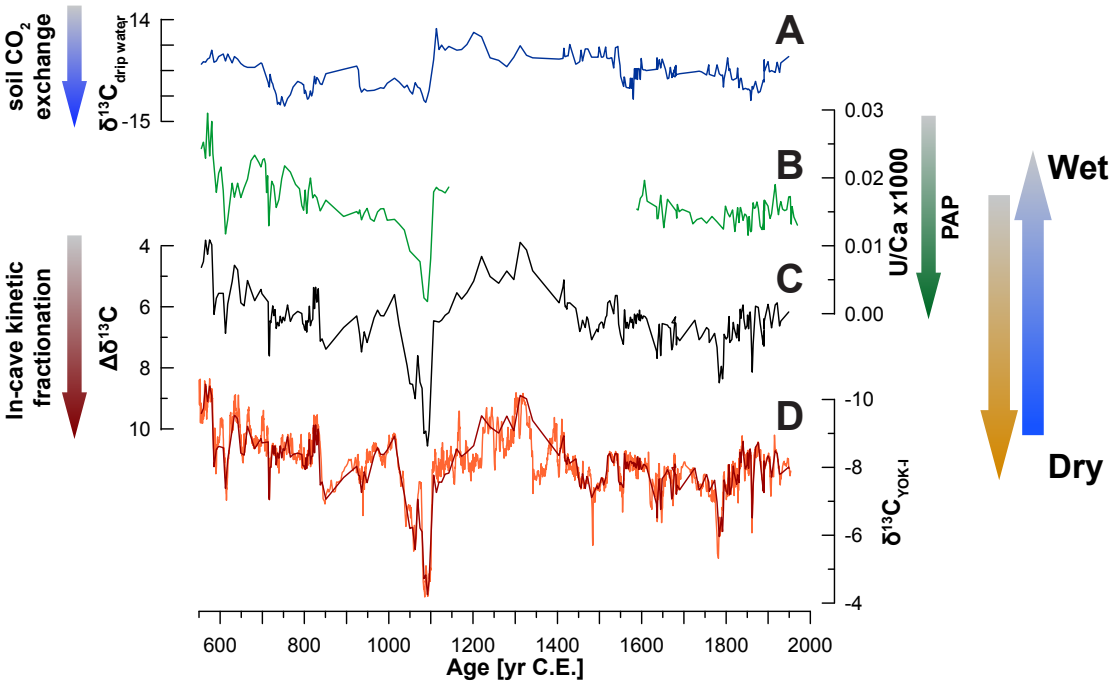

Fig. 6: Evolution of $\delta^{13}C$ in the Yok Balum karst system, determined by modeling. A - $\delta^{13}C$ of the drip water (blue line), calculated using the measured total DCF, indicating the degree of open vs. closed system and consequently soil CO_2 exchange with the aqueous solution in the karst. B - U/Ca (green line) is modulated by PAP, and shows remarkable similarity with stalagmite $\delta^{13}C$. C - $\Delta\delta^{13}C$ (black line) is calculated as the difference between $\delta^{13}C$ of the drip water and the stalagmite, and reflects the amount of kinetic fractionation affecting the sample (as described in Griffiths et al. (2012)). D - $\delta^{13}C$ in YOK-I (red line), underlain by the high resolution profile presented in Kennett et al. (2012).

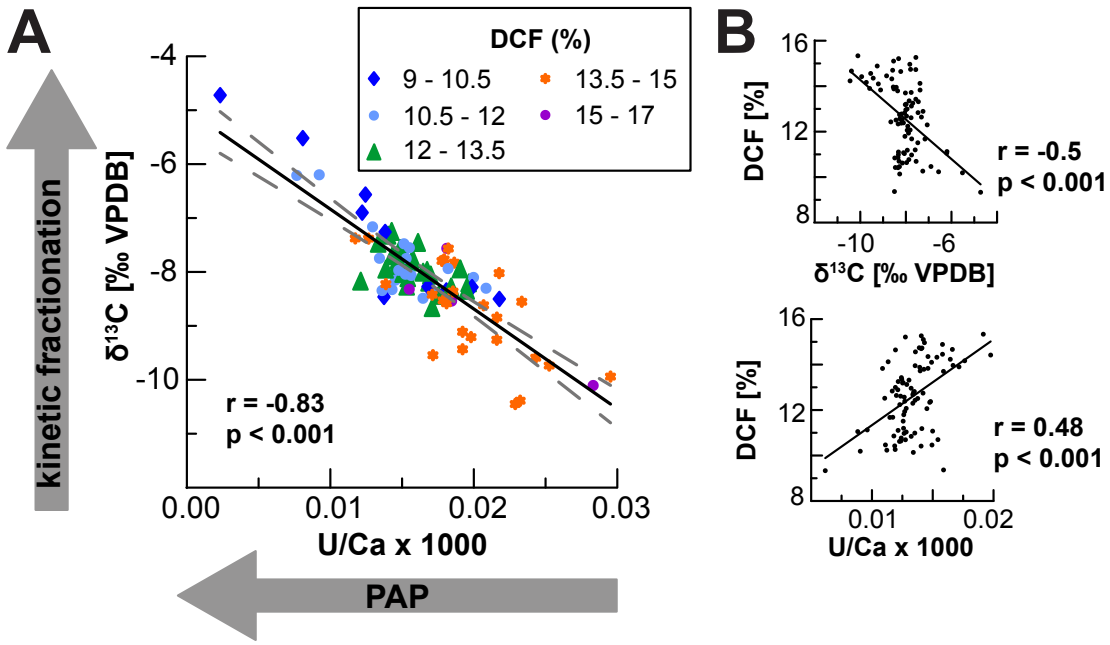

917

918 Fig. 7: Relationship between $\delta^{13}C$, U/Ca and DCF in stalagmite YOK-I: A -
919 Relationship between $\delta^{13}C$ and U/Ca. A significant linear correlation (black line, r
920 = -0.83, p<0.001; 95% confidence interval as grey dashed line) exists between
921 $\delta^{13}C$ and U/Ca ratios. DCF values are color-coded. B - Scatterplots showing the
922 relationship between DCF and $\delta^{13}C$ (upper), and DCF and U/Ca (lower), with
923 associated correlation coefficients. All proxies are influenced by karst
924 infiltration: $\delta^{13}C$ reflects the amount of PCP/PAP and kinetic fractionation in the
925 cave, whereas U/Ca is influenced by PAP. DCF responds to the degree of open-vs-
926 closed system conditions in the karst, modulated by changes in effective
927 infiltration.

928

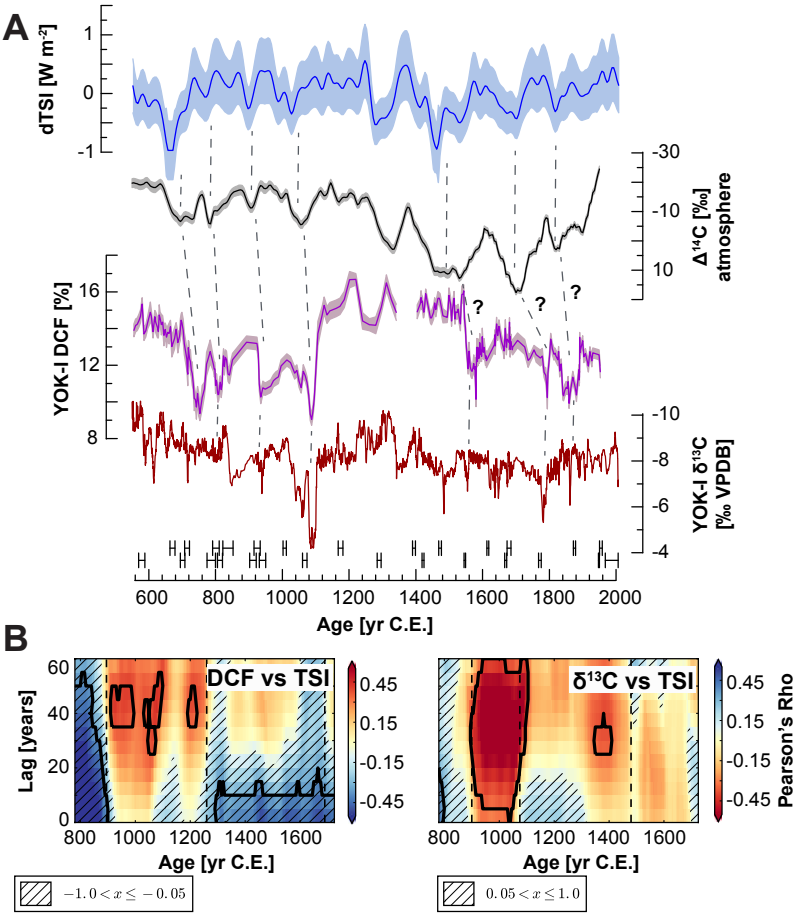

929

930 Fig. 8: External forcing on YOK-I carbon isotopic records: A - Comparison of YOK-
931 I DCF and $\delta^{13}C$ to total solar irradiance (dTSI) calculated from ^{10}Be (blue curve)
932 (Steinhilber et al., 2009) and atmospheric $\Delta^{14}C$ from IntCal13 (grey curve)
933 (Reimer et al., 2013). Dashed lines indicate features present in all records
934 suggesting solar forcing with a variable lag on precipitation at Yok Balum Cave.
935 U/Th ages for stalagmite YOK-I are shown to highlight the excellent age control
936 of the record. B - Lag-correlation plots quantifying the lag between DCF and $\delta^{13}C$
937 at Yok Balum Cave and dTSI (Steinhilber et al., 2009). The test was done with
938 5000 randomized surrogates for each lag. Dashed lines indicate significant
939 values (two-sided at 0.05 significance level with Bonferroni correction). A band
940 of high correlations lagging the solar forcing by ~30-50 years for DCF, and ~10-
941 50 for $\delta^{13}C$ is visible between ~900-1250 C.E., but the relationship breaks down

942 in the younger part of the record (1300-1700 C.E.). Note that $\delta^{13}C$ is plotted on
943 an inverse colorbar compared to DCF since the two proxies have the opposite
944 response to hydrological changes (wetter: DCF increases, $\delta^{13}C$ decreases).
945

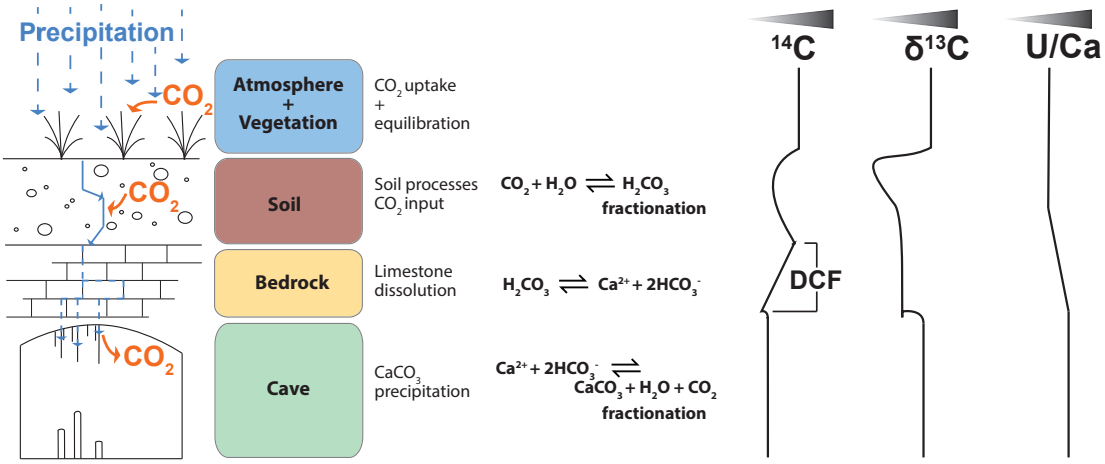

946

947 Suppl. Fig. 1: Conceptual diagram of carbon cycle processes occurring in a karst
948 system and the associated response in the hydrological proxies (^{14}C, $\delta^{13}C$ and
949 U/Ca) used in this study.
950

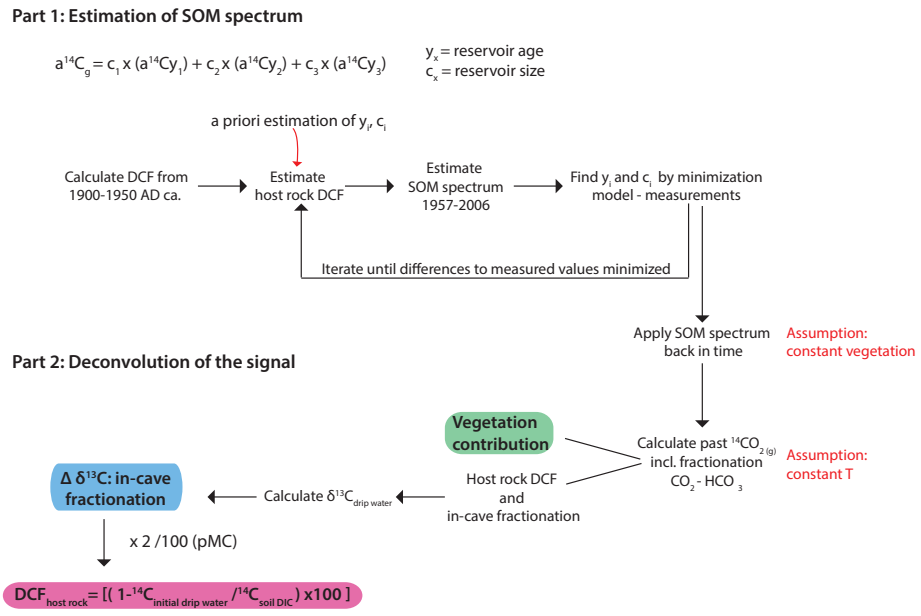

951

952 Suppl. Fig. 2: Schematic of the modeling process (as in Griffiths et al., 2012) as
953 applied to the dataset from stalagmite YOK-I. The model is composed of two

parts: in a first step, the stalagmite bomb spike is used to calculate the best fitting SOM spectrum, by using a Monte Carlo optimization process. In the second part, the SOM spectrum is applied to the remaining stalagmite dataset and the contributions to DCF from vegetation, in-cave fractionation and host rock dissolution can be separated and quantified.